Self-consistent calculations of optical properties of type I and type II quantum heterostructures

by

Vladimir A. Shuvayev

A dissertation submitted to the Graduate Faculty in Physics
in partial fulfillment of the requirements for the degree of
Doctor of Philosophy, The City University of New York

2009

This manuscript has been read and accepted for the Graduate Faculty in Physics in satisfaction of the dissertation proposal requirements for the degree of Doctor of Philosophy.

Professor Lev Deych

Date	Chair of Examining Committee

Professor Steven Greenbaum

Date	Executive Officer

Professor Igor Kuskovsky

Professor Alexander Lisyansky

Professor Vinod Menon

Professor Sergey Vitkalov

Supervisory Committee

THE CITY UNIVERSITY OF NEW YORK

Abstract

Self-consistent calculations of optical properties of type I and type II quantum
heterostructures

by

Vladimir A. Shuvayev

Adviser: Professor Lev Deych

In this Thesis the self-consistent computational methods are applied to the study of the optical properties of semiconductor nanostructures with one- and two-dimensional quantum confinements. At first, the self-consistent Schrödinger-Poisson system of equations is applied to the cylindrical core-shell structure with type II band alignment without direct Coulomb interaction between carriers. The electron and hole states and confining potential are obtained from a numerical solution of this system. The photoluminescence kinetics is theoretically analyzed, with the nanostructure size dispersion taken into account. The results are applied to the radiative recombination in the system of ZnTe/ZnSe stacked quantum dots. A good agreement with both continuous wave and time-resolved experimental observations is found. It is shown that size distribution results in the photoluminescence decay that has essentially non-exponential behavior even at the tail of the decay where the carrier lifetime is almost the same due to slowly changing overlap of the electron and hole wavefunctions. Also, a model situation applicable to colloidal core-shell nanowires is investigated and discussed.

With respect to the excitons in type I quantum wells, a new computationally efficient and flexible approach of calculating the characteristics of excitons, based on a self-consistent variational treatment of the electron-hole Coulomb interaction, is developed. In this approach, a system of self-consistent equations describing the motion of an electron-hole pair is derived. The motion in the growth direction of the quantum well is separated from the in-plane motion, but each of them occurs in modified potentials found self-consistently. This approach is applied to a shallow quantum well with the δ-potential profile, for which analytical expressions for the exciton binding energy and the ground state eigenfunctions are obtained, and to the quantum well with the square potential profile with several different well and barrier materials. The numerical results yield lower exciton binding energies in comparison to standard variational calculations, while the iterative scheme used to calculate the energies and respective wavefunctions is stable, rapidly convergent and requires reduced computational effort. Thus, the method can be an important computational tool in computing exciton characteristics in quantum wells exceeding currently existing approaches in accuracy and efficiency. The method can also be naturally generalized for quantum wires and dots.

Acknowledgments

It is difficult to exaggerate my gratitude to my Ph.D. advisers, Professors Lev Deych and Alexander Lisyansky. With their enthusiasm, their inspiration, and great efforts to explain things clearly and in a simple way, they helped me to understand the solid state physics on a deeper level. Throughout my research and thesis-writing they provided encouragement, advices, and suggestions, which made this difficult way through science really enjoyable. I would have been lost in the “jungles” of physics without them.

I am very grateful to Dr. Ilya Ponomarev, former postdoctoral fellow, and Dr. Mikhail Erementchouk, former graduate student of the Physics Department, for their support and useful discussions, which continued even after their departure from the department.

I would like to thank Professor Igor Kuskovsky, who provided experimental data for the stacked quantum dots and actively participating in discussions of the model and interpretation of the data.

Separate thanks to all members of the Physics Department of Queens College for their friendly and supportive environment during all my years at Queens and especially to Donna Hernandez, for creating home-like atmosphere at the department.

At last, I would like to express my sincere appreciation to my mother and sister. They are always a source of inspiration, love and support for me.

Contents

List of Tables

List of Figures

Chapter 1

Introduction

> *It can be said that if the possibility of controlling the type of conductivity of a semiconductor material by doping with various impurities and the idea of injecting nonequilibrium charge carriers were the seeds from which semiconductor electronics developed, heterostructures could make it possible to solve the considerably more general problems of controlling the fundamental parameters inside the semiconductor crystals and devices: band gaps, effective masses of the charge carriers and the mobilities, refractive indices, electrons energy spectrum, etc.*
>
> Z. Alferov, Nobel Lecture, December 8, 2000

1.1 Semiconductor heterostructures

In 2000 the Nobel Prize was awarded with one half jointly to Herbert Kroemer (University of California at Santa Barbara, California, USA) and Zhores I. Alferov (A.F. Ioffe Physico-Technical Institute, St. Petersburg, Russia) for "developing semiconductor heterostructures used in high-speed- and opto-electronics", and one half to Jack S. Kilby (Texas Instruments, Dallas, TX, USA) for "his part in the invention of the integrated circuit". This prize emphasized the increased interest in low-dimensional heterostructures, due to their potential for applications in various electronic and optical devices, such as transistors, diodes, lasers, detectors, solar cells, biological sensors, *etc* [see e.g. Refs. [6–12] and references therein].

The introduction of the heterostructures with two-dimensional (2D) confinement (quantum wells or QWs) in the early 1970s was a turning point in the direction of research in the field of electronic structures [13]. The new era, when the properties of the semiconductor device can be tuned rather by spacial dimentions than by the change in material composition, began. In 1980s the interest of researchers shifted toward structures with further reduced dimensionality: one-dimensional (1D) confinement (quantum wires or QWRs) [14] and zero-dimensional (0D) confinement (quantum dots or QDs) [15]. These heterostructures are formed by combination of multiple heterojunctions, although these two terms are commonly used interchangeably. Such combination results in the band discontinuities whose effect on spectrum of electrons and holes in the effective mass theory (EMT) approximation can be described in terms of effective potential wells and barriers for carriers. If the band alignment is

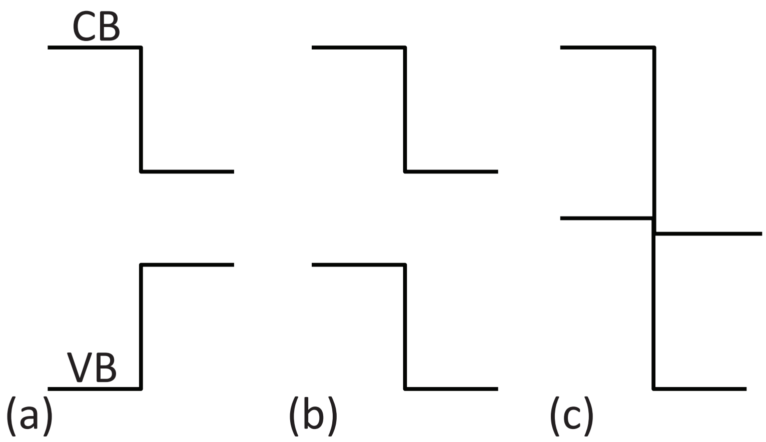

Figure 1.1: Three types of conduction (CB) and valence (VB) bands alignment at semiconductor heterojunction: (a) stradding gap (type I), (b) staggered gap (type II) and (c) broken gap (type III).

such that the minimum of the conduction and the top of the valence bands of the smaller band gap material are in the band gap region of the larger band gap material, the structure is classified as type I (Figure 1.1(a)). In such a structure the lowest electron state and the highest valence band state exists in the same physical space (in the narrow gap material). Type I heterojunctions (sometimes referred to as direct in real space structures) are the most widely used ones. A GaAs/$\mathrm{Al}_{1-x}\mathrm{Ga}_x\mathrm{As}$ system is a typical example of this kind when x, showing the fraction of atoms of a particular type [16]. Another type of band alignment, called type II, results in formation of the potential well for electrons in one material and for holes in the other (Figure 1.1(b)). As a result, electrons and holes in type II structures are spatially separated giving rise to an internal electric field that bends the conduction and valence bands and modifies energy levels and wavefunctions of electron-hole pairs. The "effective" band gap in this kind of structure (i.e., energy difference between the lowest conduction band bottom and highest valence band bandedge) can be very small and, therefore, they are very useful for long wavelength optoelectronics. Of course, one has to recognize that since the electron and hole states are spatially separated optical transitions are weak. The InP/InSb system provides a widely studied example of this band alignment [17]. The last type of heterojunction is called type III (although other names have also been given to it, such as “broken type II”) (Figure 1.1(c)) and it looks like type II, just more strongly pronounced and without band gaps overlap. The system GaSb/InAs belongs to this type.

1.2 Semiconductor excitons

1.2.1 Excitons and their types

The optical absorption of some semiconductors or insulator materials shows a series of peaks or features at photon energies close to but lower than the energy gap. These features correspond to a particular type of excitation called an *exciton*. Excitons are quasi-particles that form when Coulomb-interacting electrons and holes, created, for example, by the incident light with photon energy above the gap or exactly equal to that of the exciton, are bound into pair states and can move through the crystal and transport energy through materials without contributing to the electrical conductivity. The situation with exciton is very similar to that of a hydrogen atom (in which an electron orbits around a proton) and the hydrogenic model is often used to describe the behavior of excitons. They are thus central to our understanding of

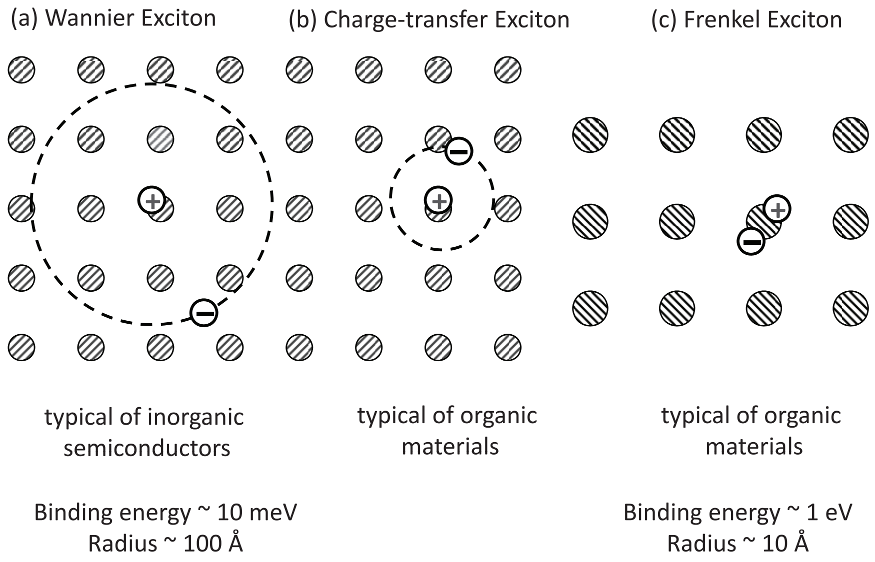

Figure 1.2: Different types of excitons and their typical properties

how light interacts with matter and in our exploitation of opto-electronic effects.

Excitons can be distinguished between two limiting cases, which depend on the properties of the materials in question. Semiconductors typically have a high value of the dielectric constant, and as a result, screening tends to reduce the Coulomb interaction between electrons and holes. This leads to the creation of the Mott-Wannier exciton [18], which has a radius much larger than the lattice spacing. Thus, the effect of the lattice potential can be incorporated into the effective masses of the electron and hole, and due to the lower masses and the screened Coulomb interaction, the binding energy is usually much less than that of a hydrogen atom, typically of the order of 0.1 eV. On opposite side, in insulators or organic materials, excitons tend to be much smaller, of the same order as the unit cell, so the electron and hole sit on the same site. This is a Frenkel exciton, named after J. Frenkel [19, 20], who predicted, gave the name and developed the theory of excitons in semiconductors. Also there is

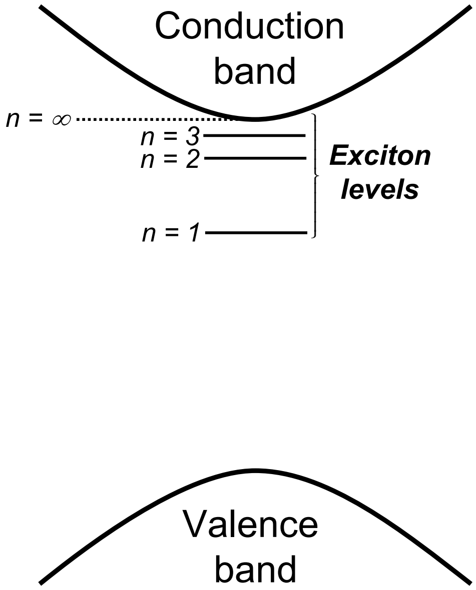

Figure 1.3: Bulk semiconductor band structure with exciton energy levels

a third type of exciton with parameters lying between the properties of the first two, so-called charge-transfer exciton, which electron and hole sit on the neighbor sites (Figure 1.2). In this Thesis we will deal only with Wannier excitons.

Band diagram with exciton energy levels is presented in Figure 1.3. Thus the total energy of the exciton in the bulk is simply the energy of the free electron - free hole pair plus the exciton binding energy E_X:

$$E_{total} = E_{gap} + E_X, \tag{1.1}$$

where $E_X = -\mu e^4/(\hbar^2 \epsilon^2 n)$ and

$$\frac{1}{\mu} = \frac{1}{m_e^*} + \frac{1}{m_h^*} \tag{1.2}$$

is the reduced mass of exciton written in terms of effective masses of the electron and hole, ϵ is the dielectric constant of the media and n is an exciton energy level.

The binding energy of the exciton, created by the electron and heavy hole, in GaAs, for example, is about 4.7 meV. Since the exciton line is broadened by background impurity potential fluctuations, as well as phonons, it is possible to see such transitions only in high purity semiconductors, at low temperatures. In fact, the observation of excitons in bulk semiconductors is a good indication of the quality of the sample.

The process of creation of excitons is a reversible one and excitons can have a short lifetime (although lifetimes up to 13 milliseconds have been observed in Cuprous oxide [21] versus lifetime of 0.22 nanoseconds in GaN [22]), at the end of which they recombine either radiatively or nonradiatively. In case of radiative recombination of the electron-hole pair a photon of a sharp spectral line is emitted, which can propagate a short distance inside the crystall creating a new exciton. In radiative band-to-band recombination the square of the electron-hole overlap, so-called oscillator strength which is inversely proportional to exciton lifetime, is a decisive factor in determining the properties of the exciton in optical experiments. At the same time, with lower transition probability, a band-to-band transition can occur together with emission of one or more optical phonons, creating photon with energy below the exciton creation energy. At low temperatures, where the exciton radiative recombination dominates, the exciton dynamics is closer to that observed in low-dimensional heterostructures, depending on the purity of the materials and surface disorders. In the presence of impurities, bound excitons may be created and their recombination will be dicussed later in current Chapter.

At high temperatures, where nonradiative recombination dominates, excitons may dissociate into free carriers when thermal energy is larger than binding energy of exciton $kT > E_X$. Nonradiative recombinations include inelastic scattering with creation of phonons and Auger recombination. In the latter process one electron-hole pair recombines and transfers all of its energy to a third particle, e.g., a free electron, as additional kinetic energy. This process can limit the quantum efficiency in high density electron hole pair systems, as an example, in laser diodes [23].

1.2.2 Excitons in heterostructures

When characteristic dimensions of heterostructures become comparable with the effective Bohr radius of excitons, one has to take into account quantum confinement of electrons and holes. An important manifestation of this confinement is increased binding energy and oscillator strength of excitons. As a result, excitonic effects in these structures are especially important for understanding of the basic optical properties as well as for the potential applications. In contrast to Eq. (1.1), the total energy of exciton in heterostructure has additional components due to the electron and hole confinement energies, i.e.

$$E_{total} = E_{gap} + E_e + E_h + E_X, \tag{1.3}$$

where E_e and E_h are electron and hole energies arising from the spacial confinement. Thus, the total exciton energy is clearly a function of structure because of the structural dependency of the confinement energies. In addition, it must be expected that the Coulomb potential energy, i.e. E_X, also depends upon the structure. This latter effect arises because the electron-hole separation can vary quite considerably between heterostructures, resulting in increasing binding energy of excitons and their oscillator strengths as one is going from bulk to quantum wells, and further to quantum wires and quantum dots.

Unfortunately, an ideal one-dimensional model leads to the the divergency of the exciton energy. However, in real quantum wires, this divergence is expected to be weakened due to the quasi-one-dimensional geometry, and the oscillator strength is distributed among the interacting electron-hole states. As the result of the confinement, in GaAs quantum wells excitons are prominent features in the optical properties at room temperature even though this is not the case in the bulk [24]. This property together with increasing perfection of fabrication technique for complex layered nanostructures make excitons very attractive for various optoelectronic applications.

In tightly confined low-dimensional systems (1D or 0D), the effective Coulomb interaction is greatly enhanced and optical transitions generally lead to the formation of strongly bound excitons. When more than one exciton is present, the Coulomb interaction also leads to rapid exciton-exciton annihilation through an Auger recombination process [25]. This effect may be significant even at low exciton densities.

In general, the most fundamental properties of the confined excitons are the confinement energy, the type of recombination process (indirect phonon-assisted or direct one), the optical transition oscillator strength.

Currently excitonic effects are of vital interest in a variety of aspects of the behavior of low-dimensional systems, including their non-linear optical properties, time-dependent and transport properties, and exciton-exciton interactions. The study of the properties of excitons in quantum well is under rapid development since the pioneering experiment by R. Dingle, et al [13] in 1974. The authors observed a characteristic step-like behavior in absorption spectra of GaAs/AlGaAs semiconductor heterostructures with ultrathin GaAs layers (QWs) and systematic shifts of the characteristic energies with a quantum well width decrease.

There are several experimental techniques for direct measurements of exciton properties. Among them are photoluminescence (PL) [3], which we briefly describe in the next Section of the current Chapter, absorption [26], and PL measurements in high magnetic fields [27]. An accurate interpretation of measured spectra in QW nanostructures requires a rigorous theory, which, on the one hand, can incorporate details of semiconductor band structure, effects of mass and dielectric mismatches, *etc.* On the other hand, a theory preferred to be practical and flexible enough to adjust quickly to various experimental situations.

Unfortunately, the problem of calculating exciton energies in a QW is untractable analytically even in the simplest model (isotropic parabolic conduction and valence bands, no valence-band mixing and dielectric and effective mass mismatches). The difficulties are caused by non-separability of electron-hole Hamiltonian: the presence of QW potential breaks the translational invariance of the system, making it impossible to separate in-plane motion of electrons and holes from the motion in the direction of growth of QW. Therefore, one has to resort to numerical calculations, and, by now, there have been developed several methods of numerical solution of the Schrödinger equation for QW excitons. Most elaborate schemes [28] take into account valence band mixing as well as non-parabolicity effects and are based on an expansion of the exciton wavefunction in terms of multicomponent envelope functions of electron and hole states and subsequent numerical solution of coupled integral equations in momentum space. Similar approaches based on a position-space expansion of the interband polarization operator in terms of complete system of single-particle eigenfunctions of the one-dimensional Schrödinger equation for the quantum well potential were developed in Refs. [29–31]. The coefficients of this expansion, which represent the unknown wavefunctions of in-plane motion, satisfy an infinite set of coupled ordinary differential equations. Such a system is solved numerically after an appropriate basis truncation. These approaches suffer from difficulties related to the unknown errors due to basis truncation.

Other approaches that have been used to obtain many of important results in this area are based on one or another version of the standard variational method [32–35], which, due to its transparency, provides basic physical insight into the problem. In this approach a certain form of the exciton wavefunction, depending on one or several variational parameters, is postulated. Usually, it is chosen in the form of a product of three terms:

$$\Psi(z_e, z_h, r; \lambda_1 \ldots \lambda_N) = \chi_e(z_e)\chi_h(z_h)\phi(r, z_e, z_h; \lambda_1 \ldots \lambda_N) \tag{1.4}$$

The first two are exact single-particle one-dimensional electron and hole wavefunctions describing their confined motion in the growth direction. The third term models the effects of the Coulomb interaction on the relative motion of an electron-hole pair. The accuracy of the results obtained within this type of calculations depends on the physical appropriateness of the latter term and its complexity, which is determined by the number of variational parameters. The more parameters are introduced in the trial function, the lower the resulting exciton energy, but, of course, the more extensive the calculations. There is ample literature dealing with accurate variational numerical calculations of exciton binding energy in quantum wells [36–44]. Most advanced of them include the effects of Coulomb screening due to dielectric constant mismatch, as well as effective mass mismatch at heterojunctions and band degeneracy [35, 36], but their application is usually limited to QW with relatively large confinement potentials, and their extension to more complex situations such as asymmetric wells or presence of external fields is not straightforward.

1.3 Radiative recombination of electron-hole pairs

Efficient radiative recombination between electrons and holes takes place only in direct band gap semiconductors. During an optical transition, momentum is conserved, and since the photon carries away negligible momentum, transitions take place only between conduction band and valence band states having essentially the same momentum. This is easily satisfied in direct band gap semiconductors. However, for indirect band gap semiconductors, the optical transitions between free electrons and holes are forbidden in dipole approximation. Radiative electron-hole recombination is possible in this semiconductors when the transition is assisted by phonons and impurities [45].

In type I QWs, where the motion of both electrons and holes is restricted to 2D planes, it is known that the lifetime becomes shorter with the decrease of the well width as a result of squeezing of the exciton internal motion [46]. In type I QDs, where the motion of electrons and holes is restricted in all three dimensions, the lifetime is supposed to become shorter as the dot size increases, because the magnitude of the oscillator strength of the radiative recombination is enhanced with increase of the so-called “exciton coherence volume” [47]. It is commonly assumed that the impact of confinement dimensionality on the lifetime manifests itself most clearly in the thermal variation of the lifetime. The lifetime generally shows a linear increase in QWs [46, 48] and a square root increase in QWRs [48] with temperature, while such thermal effect is expected to be suppressed in QDs [49].

1.3.1 Recombination on optical centers

Free carriers and excitons in semiconductors can be trapped at donors or acceptors in either neutral or ionized states and subsequently recombine, annihilating the electron-hole pair.

These point defects or optical centers can be separated into charged (donor or acceptor) and neutral (“isoelectronic”) centers, with the main difference between them expressed in the presence or absence of the Coulomb potential. The ground state of the donor center has one excess electron, resulting in the net negative charge at the defect region, while a single acceptor has a net positive charge. On the contrary, the isoelectronic center does not have net charge in the local bonding region. However, the hole or electron can be localized at such center by a local potential and may capture the second particle by the Coulomb attractive field into the shallow state [50], which can be described by EMT. This simple description fits not only a single center, but also complex defects involving more than one site [51].

The excited state in the charged defects can be usually described with the help of the EMT approximation [52, 53] based on the hydrogen-like Coulomb potential. In case of the localization of excitons at these centers, they create a bound exciton (BE) excitation, consisting of three carriers bound to a charged impurity (Figure 1.4(a)). Due to the strong localization of these carriers in the small region of a real space, an Auger transition can occur. Auger transitions are believed to limit the lifetimes of the BEs in many cases [54].

Vice versa to the charged centers, the isoelectronic centers do not have any charged particle localized in the ground state, and, therefore, the analog of excitations mentioned earlier does not exist. Such centers bind charged particles by a weak interaction resulting from the strain field or from a local change of the electronegativity, although the cross section for capture of the first particle is quite small. After trapping of the first particle, the second carrier, with opposite sign of the charge, can be attracted by the Coulomb field produced by the first particle (Figure 1.4(b)).

The radiative decay of the excitons bound to the isoelectric centers is an important physical process in the semiconductors. This is especially true for the indirect semiconductors, where direct band-to-band transitions are forbidden by the $\overrightarrow{k}$-conservation rule. Insertion of the isoelectric impurities into this type of semiconductors helps to improve the quantum efficiency of optical emission. Emission due to the exciton recombination at the isoelectric center is characterized by a long radiative decay time with lifetimes $\tau > 10^{-6}$ seconds [55], which implies stability and high radiative efficiency comparable to the nonradiative Auger processes [56]. As a result of the weak binding of the electron and hole, the energy of the luminescence photon is

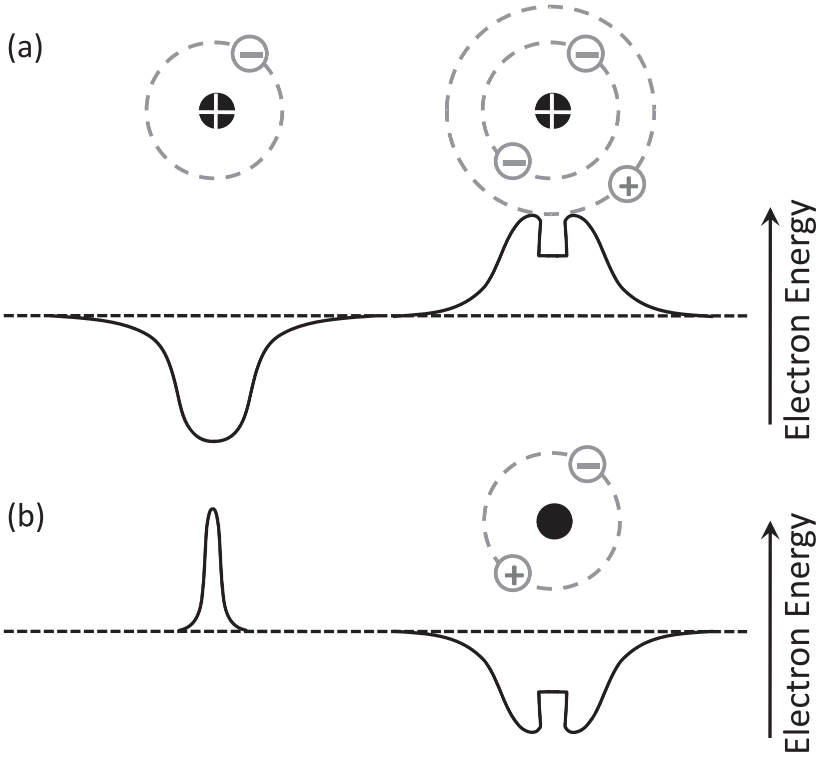

Figure 1.4: Schematic single particle potentials of the ground and BE states of (a) a single donor and of (b) an isoelectronic donor center (for initial particle at the left and for the secondary particle at the right). Acceptor potentials could be obtained by swapping of sign for charged particles and potentials.

below the gap, but relatively smaller than that of the exciton bound to shallow donor or acceptor. The isoelectronic bound excitons (IBEs) are the subject of technological interest due to the possible intense room temperature emission as the result of high exciton binding potential.

1.3.2 Photoluminescence

Spontaneous emission of light from a material under optical excitation is called radiative photoluminescence (PL). The emission spectra of the PL is produced by the various ways of subsequent recombinations of the electron-hole pairs and transitions from the excited states to the lower states. Parameters of the excitation, such as intensity and energy, can be used to probe different excitation types at different spatial parts of the sample. Measurements of the PL allow to characterize a set of material parameters and to obtain values of the energy states at the surfaces, interfaces and impurities. Experiments with pulsed excitation source (time-resolved PL or TRPL) provide information about lifetimes of the excited states. Moreover, although the photoluminescence is produced by radiative processes, the thermally activated non-radiative recombinations are affecting the PL, thus allowing to investigate them in this indirect way.

Some of the main advantages of the PL are a generally nondestructive interaction with the sample and a very small necessity in manipulation over sample or environment. Illumination of the material with light creates electron-hole pairs or excited electronic states depending on the energy of the photon. These excitations are relaxing to the ground state or electron-hole pairs recombine with time. The PL spectra reveals these transition energies and provides information about rates of radiative and nonradiative recombinations or transitions.

PL spectroscopy can be generally separated into few types. Those experiments, which are performed under fixed excitation energy, generally used to obtain information about luminescence properties. If the detection energy is fixed (photoluminescence excitation spectroscopy or PLE), then it is possible to gather information about absorption properties and to probe the excited states of the optical centers. In case of the narrow spectral lines, observed in optical transitions, the magneto-optical spectroscopy, or Zeeman spectroscopy, can be used. It requires the low temperature sample in the high magnetic field with good optical access for the excitation radiation.

The effect of modification of the electron-hole pair energy levels and wavefunctions in the type II heterojunction, due to the bending of the bands, is manifested in both "continuous wave" (CW) and time-resolved photoluminescence: in the former it is responsible for the blue shift of the photoluminescence with increasing excitation intensity [57–62], whereas in the latter it results in a relatively long (due to weak overlap of the wavefunctions) non-exponential decay [57, 60, 61], which also depends on the excitation intensity [57, 60–62]. The non-exponential decay is often considered by fitting experimental results to multi-exponential [63] or stretch-exponential [64] functions with fitting parameters having little if any physical meaning. There have been a number of attempts to obtain a quantitative description of this behavior in type II quantum wells using self-consistent Poisson-Schrödinger analysis [57] or microscopical multiband semiconductor luminescence equations [62].

While the shift of the PL with pumping intensity for type II nanostructures has been extensively discussed in the literature, the time evolution of the PL has attracted much less attention. Although there are works where PL lifetime has been calculated as a function of the photo-excited carrier concentration and PL kinetics in quantum wells was compared with experiment [see e.g., Refs. [57, 65]], we are not aware of any work related to the structures with cylindrical symmetry and dispersion of the geometrical parameters.

1.3.3 Recombination and transition rates

The emission of light during recombination of the electron-hole pair or transition of the charge carrier from initial state "i" to the final state "f" is a scattering event induced by the time-dependent perturbation $\hat{H}$ [66]. The transition rate could be described by the Fermi's Golden Rule [10]:

$$\frac{1}{\tau_{i\to f}} = \frac{2\pi}{\hbar} \left| \langle\psi_f| \hat{H} |\psi_i\rangle \right|^2 \delta(E_f - E_i \pm \hbar\omega), \tag{1.5}$$

where the upper sign in ± corresponds to the emission process and the lower sign corresponds to the process of photon absorption; ψ_f and ψ_i are the envelope wavefunctions of the final and initial state, correspondingly.

The momentum of the photon is assumed to be zero or negligibly small, thus there is no need in additional delta function for momentum conservation and all transitions on the band diagrams are always vertical whether they are between different bands (interband) or within the same band (intraband or itersubband).

Although a lot of results in physics of condensed matter are obtained within the envelope function approximation, here it is necessary to use the rapidly varying component of the wavefunction, or Bloch function u, writing the whole wavefunction as a product of these two terms $u\psi$. The concepts of the Bloch state and Bloch function were developed by F. Bloch in 1928 in order to describe the conduction of electrons in crystalline solids [67]. Using this description of the wavefunction it can be shown [10] that the matrix element in Eq. (1.5) becomes:

$$\langle u_f\psi_f| \hat{H} |u_i\psi_i\rangle = \langle u_f| \hat{H} |u_i\rangle_{cell} \langle\psi_f|\psi_i\rangle + \langle u_f|u_i\rangle_{cell} \langle\psi_f| \hat{H} |\psi_i\rangle, \tag{1.6}$$

where index "cell" corresponds to the unit cell of the crystalline lattice. In the case of interband transitions between the conduction and valence bands the functions u_f and u_i are orthogonal as the Bloch functions from different bands at the same point of the Brilloiun zone and Eq. (1.6) transforms into:

$$\langle u_f \psi_f | \hat{H} | u_i \psi_i \rangle = \langle u_f | \hat{H} | u_i \rangle_{cell} \langle \psi_f | \psi_i \rangle . \tag{1.7}$$

Hence, for the interband transitions, the envelope function overlap integral $\langle \psi_f | \psi_i \rangle$ determines allowed and forbidden transitions together with changes in the transition rates upon modification of the investigated system with unchanged materials.

In the case of intersubband transitions between the energy levels within the same band the envelope functions ψ_f and ψ_i are both eigenfunctions of the same Hermitian operator and are orthogonal to each other. Therefore, matrix element now transforms into:

$$\langle u_f \psi_f | \hat{H} | u_i \psi_i \rangle = \langle u_f | u_i \rangle_{cell} \langle \psi_f | \hat{H} | \psi_i \rangle . \tag{1.8}$$

Interband radiative transitions play important role in light sources [10] and detectors [11]. Applicability of this mechanism is very wide due to the possible tuning of the spectra from the near infrared to the blue region by proper selection of the materials or parameters of the heterojunction.

1.4 Main objectives of this Thesis

The main objectives of our research is to study numerically optical properties of several types of semiconductor heterostructures with quantum confinements. Our attention is mostly focused on systems with two-dimensional (quantum wells) and one-dimensional (quantum wires) quantum confinements. Some results of our calculations are also used to discuss experimental data obtained for vertical stacks of quantum dots, which are nominally zero-dimensional structures, but when arranged in vertical heterostructures demonstrate one-dimensional behavior due to inter-dot tunneling coupling of electrons and good confinement of holes.

As an example of one-dimensional structure, in the next Chapter we consider type II cylindrical quantrum wires, which present an interest as detectors of infra-red radiation as well as for other applications. As it was pointed out in Introduction, type II structures are characterized by spatial separation of electron and holes residing in different materials. Therefore, excitonic effects in such structures are small and can be neglected. However, other many-particle effects such as band bending due to electric field produced by excited carriers become important. Thus our main objective in this part of the Thesis is to study dependence of electron and hole energies and wavefunctions on the number of photoexcited carriers. We achieve this objective using Hartree [68] approach, which include solving self-consistently the system of Schrödinger and Poisson equations. An important distinction with earlier studies of this problem consists in taking into consideration not only electrons and holes occupying lowest lying sub-bands, but also a possibility of a non-zero population of higher lying sub-bands. The results of these calculations are used to model dependence of photoluminescence spectra energies on the excitation intensity as well as behavior of time-resolved PL. In the latter case, we take into account that the experimentally observed non-exponential tail in the time dependence of the PL may be caused not only by modifications of the electron-hole states dependent on excitation intensity, but also by random variations in geometric characteristics (e.g. size) of nanostructures. Such a dependence on geometry arises because in a typical PL experiment the signal is collected from a large number of nanostructures. Here we take into account effects of the disorder by directly averaging calculated intensity of emission over a statistical distribution of the parameters of the considered structures, following the approach of Ref. [69]. Taking into account both effects contributing to the non-exponential PL decay enables us to carry out more accurate comparison of our calculations with experimental results.

While our calculations most directly apply to quantum wires and we make several conclusions regarding manifestation of studied effects in colloidal core-shell quantum wire structures, with a small modification they can also be used to study different types of structures. In particular, we use our approach to describe vertically stacked self-assembled quantum dots with close to a circular cross section, on which were performed CW and time-resolved PL measurements. Although this system differs from quantum wires, we show that under certain circumstances we can easily adopt our theory by introducing an anisotropic effective mass for holes. The results of these studies are summarized in Chapter 2 of this Thesis.

In Chapter 3 we present our results related to the properties of type I quantum wells. In these structures excitonic effects are not negligible, therefore, the main focus of our research in this area is to develop more efficient methods of calculating exciton binding energies and wavefunctions in such structures. Our approach is again based on ideas of Hartree method [68], but in its different reincarnation.

Our approach is based on presentation of the exciton wavefunction in the form of the products of three functions, each dependent on its own set of coordinates, and then using variational principle to obtain self-consistent equations for these functions. Unlike previous variational approaches we do not postulate any apriori form of the trial functions, finding them instead from the self-consitent set of equations. In our system of equations motion of the electrons and holes in the direction perpendicular to the quantum well plane is separated from the relative two-dimensional in-plane motion of the exciton. The latter one is described by a self-consistent Coulomb potential averaged with the wavefunctions of electron's (hole's) motion in the confinement direction, which depend on the effective confinement potential and are also determined self-consistently. Wavefunctions and effective potentials are determined self-consistently. Effective confining potential is a combination of the original quantum well potential and averaged Coulomb potential. In this case we have non-perturbative mixing of electron and hole subbands which, as we expect, will give more accurate results. The developed technique is applied to the case of shallow δ-potential quantum well and to the square quantum well which exhibits both mass and dielectric constants mismatches. Previous attempts to treat the Coulomb term in Hamiltonian in a self-consistent manner have been made in Refs. [30, 31, 43, 44, 70–72].

Additional details of the calculations carried out in this work are provided in Appendices A-C.

Chapter 2

Type II quantum wires and stacked quantum dots

Interest to the quantum wires with type II band alignment is particularly stimulated by recent advances in fabrication technologies that led to development of several growth techniques allowing synthesizing QWRs composed of two single-crystalline semiconductor materials with core-shell, core-multishell, or superlattice-like structures [73, 74].

In this Chapter we introduce a model, applicable to the type II (core-shell) quantum wires, describe details of calculations and provide more detailed arguments justifying applicability of our results to vertically stacked quantum dot structures. Also we give details of the experimentally studied structure and compare theoretical data with experimental results.

2.1 Theoretical model

Our theoretical analysis is based on an assumption that electron-hole pairs created by an optical pulse with the photon energy above the largest band gap rapidly relax into the lowest available states by non-radiative processes, where they reach a quasi-equilibrium with the lattice before they recombine radiatively. Therefore, populations of electrons and holes can be characterized by the Fermi distributions with two independent chemical quasi-potentials. The goal of theoretical calculations in this situation is to find the electron and hole Fermi levels as functions of the number of excited electron-hole pairs. To this end we solve the Schrödinger equations for electrons and holes with Coulomb interaction taken into account within a Hartree approximation [68], by adding an electrostatic potential, $\phi(r)$, determined self-consistently from the Poisson equation, to the confinement potential. The nanostructure under consideration in our model is taken as an infinitely long cylindrical type II core-shell quantum wire with shell radius r_s, and core radius r_c.

In our calculations we neglect exciton corrections to energies of electron-hole pairs, which is justified due to very small exciton binding energy for these structures (between 2 and 8 meV [61]). Taking into account the mass mismatch effect, but neglecting valence-band mixing, non-parabolicity of the conduction band, and omitting the exchange-correlation potential, the one-particle Hamiltonian in cylindrical coordinates with polar axis z in the growth direction, is given by

$$\hat{H}_j = -\frac{\hbar^2}{2}\left[\frac{1}{r}\frac{\partial}{\partial r}\left(\frac{r}{m_j^*}\frac{\partial}{\partial r}\right) + \frac{1}{m_j^* r^2}\frac{\partial^2}{\partial \theta^2} + \frac{1}{m_{z,j}^*}\frac{\partial^2}{\partial z^2}\right] + V_j(r) + q_j\phi(r), \tag{2.1}$$

where r, and θ, are respectively radial and azimuthal coordinates, index $j = e, h$

here and throughout this Chapter refers to electrons and holes respectively, q_j is the charge of the particle with $q_h = e$ and $q_e = -e$ with e equal to the electron's charge value. m_j^* stands for electron and hole radial effective masses, while $m_{z,j}^*$ introduces the vertical effective mass. Spatial confining potentials of the conduction and valence bands, V_j, radial effective masses, and the electrostatic potential, ϕ, depend on the radial coordinate only. The radial effective mass and confining potentials are finite step-like functions with jumps at r_c. In general, in what follows indexes c and s are used to designate *core* and *shell* parameters, respectively.

The omitted exchange-correlation potential term of many-electron system could be treated in the local-density approximation (LDA) of the Kohn-Sham density-functional theory (DFT) [75]. Contribution of the exchange part of the potential is well known [76], while the correlation part could be obtained with the help of the parametrized Monte-Carlo simulations [77].

In many works dealing with heavily doped structures holes are excluded from consideration [78–80], and are replaced by a fixed spatial distribution of the dopants. Such an approach is only justified when the processes under consideration are determined only by one type of carriers. In the case of not intentionally doped structures, similar to one considered in this Chapter, the heavy holes significantly contribute to the non-uniform carrier distribution, affecting the potential profile of the structure. Therefore, in this case one has to self-consistently solve both the electron and hole Shrödinger equations, which are coupled through the Poisson potential ϕ.

We separate variables in the Shrödinger equations corresponding to the Hamiltonian by presenting the wavefunction in the form

$$\Psi_{j,m_j,n_j}(r,\theta,z)=\frac{\psi_{j,m_j,n_j}(r)}{\sqrt{2\pi L_z}}e^{im_j\theta}e^{ik_jz} \tag{2.2}$$

where m_j is the azimuthal quantum number, n_j is a radial quantum number, k_j is a wave vector of free motion along z direction, and L_z is the normalizing length of the wire. At the exterior interface between the shell and vacuum we set $\psi_{j,m_j,n_j}(r_s)=0$, which corresponds to the requirement that the electrons and holes are confined to the volume of the core-shell structure.

The Poisson equation determining the electrostatic potential ϕ for given electron and hole charge densities in undoped materials is given by

$$\frac{1}{r}\frac{\partial}{\partial r}\left(\epsilon(r)r\frac{\partial}{\partial r}\right)\phi=-\frac{e\left(n_h(r)-n_e(r)\right)}{\epsilon_0}, \tag{2.3}$$

where $n_e(r)$ and $n_h(r)$ are the electron and hole volume concentrations, which are assumed to depend only on the radial distance r, $\epsilon(r)$ and ϵ_0 are permittivities of the heterojunction and free space, correspondingly. With $\epsilon(r)$ depending on radial coordinate the effect of the mismatch of dielectric constants is also taken into account. The carrier concentrations are determined by spatial distributions of the wavefunctions of respective quantum states:

$$\begin{aligned} n_j(r) &= \frac{1}{2\pi}\sum_{m_j,n_j}\left|\psi_{j,m_j,n_j}(r)\right|^2\int\limits_{E_{j,m_j,n_j}}^{\infty} f(E)g^{c,s}_{j,m_j,n_j}(E)dE, \\ g^{c,s}_{j,m_j,n_j}(E) &= \frac{1}{\pi\hbar}\sqrt{\frac{2m^{*c,s}_{z,j}}{E-E_{j,m_j,n_j}}} \end{aligned} \tag{2.4}$$

where summation is carried out over all partially filled bands, $g_{j,m_j,n_j}(E)$ is the 1D density of states at the n_jth sub-band, $f(E)$ is the Fermi-Dirac distribution function,

E_{j,m_j,n_j} are the bottom (top) energies of the respective electron and hole sub-bands. Our calculations showed that for experimentally relevant pumping intensities we can only consider ground state with $m_j = 0$, $n_j = 0$, and two closest in energy degenerate excited states with $m_j = \pm 1$, $n_j = 0$. Limiting the contribution to the charge densities only by the carriers in these states we rewrite Eq. (2.4) (omitting indexes $n_j = 0$) as

$$n_j(r) = \frac{|\psi_{j,0}(r)|^2}{2\pi} \int\limits_{E_{j,0}}^{\infty} f(E) g_{j,0}^{c,s}(E) dE + 2\frac{|\psi_{j,1}(r)|^2}{2\pi} \int\limits_{E_{j,1}}^{\infty} f(E) g_{j,1}^{c,s}(E) dE, \tag{2.5}$$

where $E_{j,0}$ and $E_{j,1}$ are the ground and the first excited states energies of the electron or hole, $\psi_{j,0}$ and $\psi_{j,1}$ are the wavefunction of the ground and first excited states, corresponding to the lowest state at $m_j = 0$ and $m_j = \pm 1$; factor 2 in the second term is due to the double degeneracy of the first excited state having the same energy for $m_j = -1$ and $m_j = 1$. At zero temperature ($T = 0$ K) distribution $f(E)$ transforms into the step function and integral over E is bounded at the upper limit by the value of the quasi-Fermi energy $E_{j,F}$. For overall electrically neutral QWR the number of electrons equal to the number of holes, $N = N_e = N_h$; thus the linear density of the carries $n_L = N/L_z$ is related to the charge distribution as

$$n_L = \frac{2\sqrt{2}}{\pi\hbar} \left(\mu_{j,0} \sqrt{E_{j,F} - E_{j,0}} + 2\mu_{j,1} \sqrt{E_{j,F} - E_{j,1}} \right), \tag{2.6}$$

$$\mu_{j,l} = \sqrt{m_{z,j}^{*c}} \int\limits_{0}^{r_c} |\psi_{j,l}(r)|^2 r dr + \sqrt{m_{z,j}^{*s}} \int\limits_{r_c}^{r_s} |\psi_{j,l}(r)|^2 r dr, \tag{2.7}$$

where $\mu_{j,l}$ is a geometric average of the square root of the electron or hole effective mass arising from the mass-mismatch effect. The second term in Eq. (2.6) should be omitted while the respective quasi-Fermi levels $E_{j,F}$ remain below the first excited state, $E_{j,1}$. In our calculations we do not introduce an additional surface charges that can arise at the interfaces between core and shell as well as between shell and vacuum due to impurities and defects. Therefore, we do not use Fermi-level pinning boundary conditions assumed, for instance, in Ref. [79]. Positions of the electron and hole quasi-Fermi levels are determined in our approach by charge neutrality condition $N_e = N_h$ and Eq. (2.6), which relates the Fermi levels to the number of photoexcited electron-hole pairs.

When solving the Poisson equation we assume zero electric field (constant potential) in vacuum outside of the structure with the zero value of the potential chosen at the core-shell interface. It should be noted that we carry out full electrostatic calculations taking into account contributions of both electrons and holes self-consistently. This circumstance distinguishes our calculations from earlier works [81, 82], where the modification of the confining potential due to the carriers was neglected within the core region, and the blue shift of the luminescence was explained only by modification of energy levels of the major carriers in the shell region due to formation of triangular quantum wells. Our calculations demonstrate that these approximations, at least for the structure considered here, are not justified, and that modification of the potential in the core region and the shift of the hole energy levels play important roles in the phenomena under study.

2.2 Self-consistent solution of the Schrödinger-Poisson system of equations

The self-consistent calculations are carried in the following repeated steps. At the initial step the electrostatic potential is equal to zero everywhere, i.e. $\phi(r) = 0$. One-particle electron and hole wavefunctions calculated from Eq. (2.1) are used to provide the carrier concentrations as functions of radial coordinate to the Poisson equation (2.3). As long as the quasi-Fermi level is below the first excited state, the second term in Eq. (2.6) is dropped and the Fermi level is given by the following expression

$$E_{j,F} = E_{j,0} + \frac{\hbar^2 n_L^2 \pi^2}{8\mu_{j,0}^2}. \tag{2.8}$$

If, however, its value, obtained in the one level approximation, grows above the first excited state, the second term in Eq. (2.6) is taken into consideration, and the value of the Fermi energy is given by a different expression

$$E_{j,F} = E_{j,0} + \frac{\left(\hbar n_L \pi \mu_{j,0} - 2\mu_{j,1}\sqrt{(\hbar n_L \pi)^2 - 8(E_{j,1} - E_{j,0})(\mu_{j,0}^2 - 4\mu_{j,1}^2)}\right)^2}{8(\mu_{j,0}^2 - \mu_{j,1}^2)^2} \tag{2.9}$$

When a new electrostatic potential is calculated, it is substituted into the Schrödinger equation (2.1) and the next iteration of the self-consistent calculations continues until the convergence criteria (variation of the potential profile from iteration to iteration is smaller than a required value) is satisfied. This scheme is described in the flow chart shown in Figure 2.1. Typically, convergence is established after $2 - 50$ iterations, depending on the parameters of the materials in the heterojunction, the number of the excited carriers and the uniformity of carrier distribution. If necessary, the

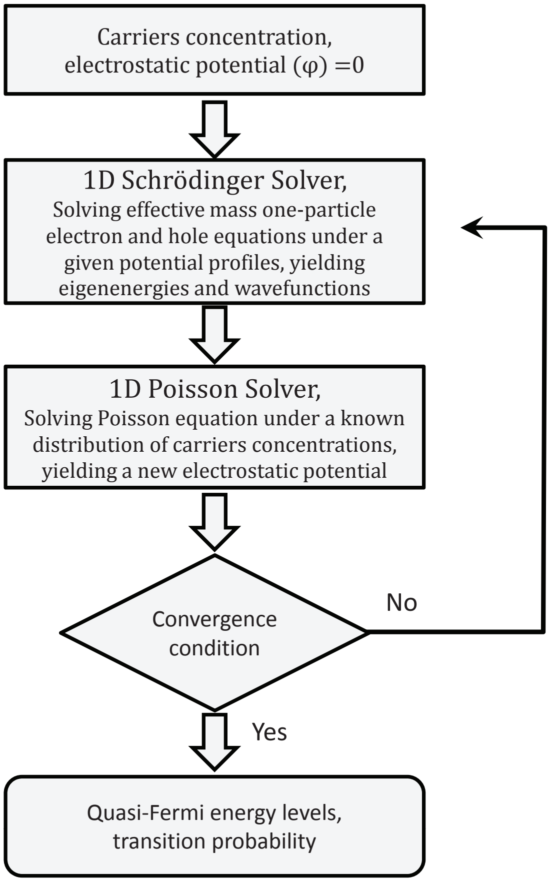

Figure 2.1: Flow chart of the self-consistent solution of the Schrödinger equation and the Poisson equation.

convergence of the procedure can be improved, for instance, by taking the electrostatic potential $\phi(r)$ at a given iteration step as an average of the electrostatic potentials obtained from the previous two iterations.

However, a serious problem with convergence of this scheme arises when one attempts to compute energy levels lying just below the top of the potential well. In this case, even if after a number of iterations the calculated energy levels remains inside the well reproducing type II type of behavior, there is a chance that at the next step it will become slightly greater than the height of the well. In this situation the particle is pushed out across the interface into the second constituent material of

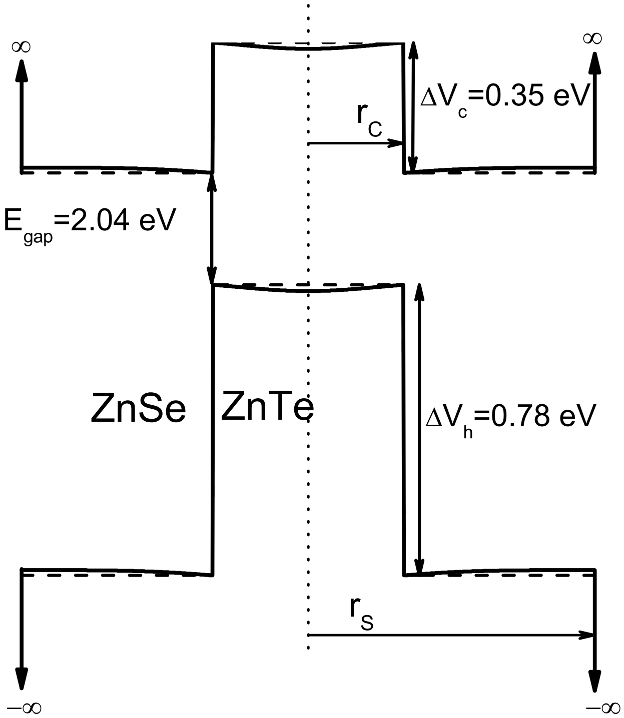

Figure 2.2: Band energy diagram of the ZnTe/ZnSe type II core-shell quantum wire with core radius 50 Å and shell radius 150 Å. Dashed lines represent the diagram in the absence of the free carriers, for which the electron ground energy $E_{e,0} = 19$ meV and the hole ground energy $E_{h,0} = 13$ meV. Solid lines are the potential profiles for linear density $n_L = 7\text{x}10^7$ m^{-1} with $E_{e,0} = 31$ meV and $E_{h,0} = 24$ meV. Energy values are counted from the bottom of each unaffected well. All profiles are in scale except of the gap between conduction and valence bands.

the heterostructure resulting in large overlap of the wavefunctions similar to type I heterostructures. Without the large initial separation between the carriers, the electrostatic potential reduces drastically, lowering the energy of the particle and pulling it back in its residence material. As a result, the system becomes “trapped” into a bistable state with two energy levels alternating at every iteration. This bistability, however, is an artifact of the computation method and does not correspond to any real physical effect. In our calculations this problem did not arise for moderate pumping levels and selected parameters of the materials. When the self-consistent

Table 2.1: Material parameters used in calculations. Here m_e^* is a mass of the electron in conduction band, m_h^* - mass of the heavy hole in radial direction and m_0 is a free electron mass. Masses and dielectric constants are taken from Ref. [1] and energy values are taken from Refs. [1, 2]

Material	m_e^*	m_h^*	ϵ	E_{gap}	ΔV_e	ΔV_h
ZnTe	0.122 m_0	0.60 m_0	10.3	2.39 eV	0.35 eV	0.78 eV
ZnSe	0.160 m_0	0.75 m_0	8.60	2.82 eV		

solution is found, the final potential profile, wavefunctions, electron and hole densities and further information can be derived. The pumping intensity in our calculations was limited by the requirement that the value of the quasi-Fermi energy level (2.8) does not exceed the second excited state. The energy of this state is obtained from Eq. (2.1) by choosing the lower of two possible levels: the lowest state for angular quantum number $m_j = 2$ or the second lowest state for $m_j = 0$ in the potential created by the converged solution of the system.

2.3 Numerical results for core-shell quantum wire

2.3.1 Modification of the conduction and valence bands

The results of our calculations for a ZnTe/ZnSe 1D structure using set of typical parameters (Table 2.1, where m_h^* refer to effective mass of the holes in the radial direction) are shown in Figure 2.2 and Figure 2.3.

First of these figures shows modifications of the potential profile due to photo-excited carriers for the radius of the core (ZnTe) $r_c = 50$ Å and radius of the shell (ZnSe) $r_s = 150$ Å. One can see that the potential profiles for both electrons and holes experience comparable modifications, which manifest in the shift of the ground

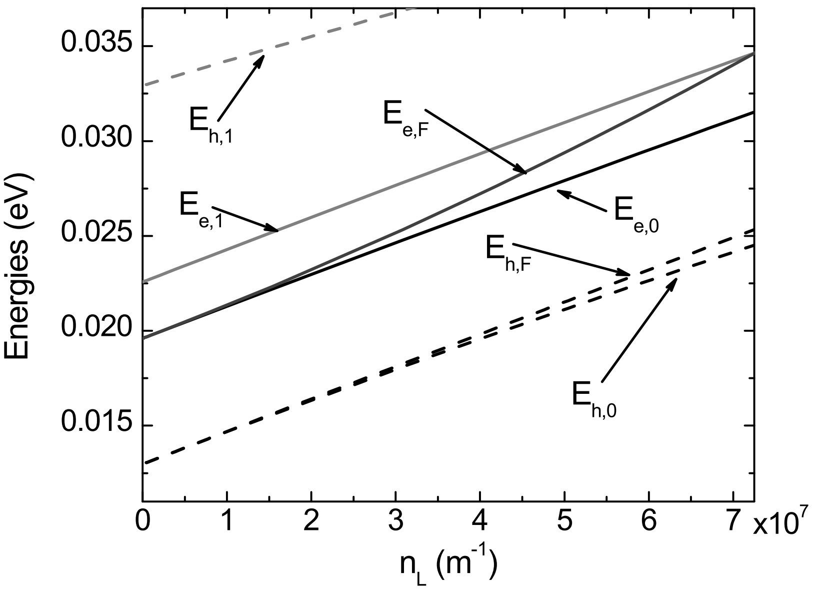

Figure 2.3: Dependence of the energies of the ZnTe/ZnSe type II core-shell quantum wire (r_c = 50 Å and r_s = 150 Å) on the density of the carries. The gap energy is not added. The maximum value of the density is limited by the condition for the quasi-Fermi level to be below the first excited state. The solid curves represent the electron energy levels: ground state, quasi-Fermi state (black) and first excited state (grey). The dashed curves are showing the same for holes. Hole quasi-Fermi energy level is shown for the same mass of the hole along the z direction as the mass along radial direction.

state energies for both types of carriers by about 10 meV. Plots in Figure 2.3 give more detailed description of the dependence of energy characteristics of electrons and holes on the number of excited pairs. First of all we shall note that the deviation of the quasi-Fermi level of holes from $E_{h,0}$ is very small even when the vertical effective mass of the holes is chosen equal to the in-plane mass. The electron quasi-Fermi level, on the contrary, depends quite significantly on the number of electrons, and one can see that at some level it exceeds the energy of the second excited level of the electrons. The main qualitative conclusion of these calculations is that the non-uniform distribution of the holes in these samples and its modification with the concentration of the carriers significantly affects the potential profile and energy levels of the electron-hole pairs and, therefore, has to be taken into account.

Having found the quasi-Fermi levels for electrons and holes as functions of the total number of electron-hole pairs, we can model the pumping intensity dependence of the emitted photon energy, which obviously has its value between maximum and minimum energies:

$$\begin{aligned} \hbar\omega_{max} &= E_{e,F} - E_{h,F} + E_{gap}, \\ \hbar\omega_{min} &= E_{e,0} - E_{h,0} + E_{gap}, \end{aligned} \tag{2.10}$$

where E_{gap} is defined in Figure 2.2.

2.3.2 Time-dependence of luminescence intensity

We analyze the time-dependence of luminescence assuming that only electron and hole sub-bands originating from their respective ground states with $m_j = 0$ are populated and that the radiative recombination occurs between electron and holes these states. In typical luminescence experiment a collected signal is produced by a large number of individual heterostructures. Unavoidable technological variations in the radii of our core-shell structures affect the rates of radiative recombination and hence the kinetics of luminescence. In our study we have considered, for the first time, combined effect of disorder and carrier population on time-resolved luminescence. Neglecting changes in the number of electron-hole pairs due to non-radiative recombination (case of low temperature), kinetics of the number of carriers is described by a simple equation

$$\frac{dn_L(r_c, r_s, t)}{dt} = -\frac{n_L(r_c, r_s, t)}{\tau(r_c, r_s, n_L)}, \tag{2.11}$$

where τ^{-1} is the rate of the radiative spontaneous recombination of the electron-hole pairs. In this equation we explicitly indicate the dependence of the carrier density and τ on the radii of the core-shell structure anticipating subsequent averaging over their distributions. The rate is given by the Fermi Golden Rule [see Section 1.3.3], assuming that the conduction band is filled up to its quasi-Fermi level and the valence band is empty up to its own quasi-Fermi level:

$$\tau(r_c, r_s, n_L)^{-1} = R\left|\langle\psi_{e,0}|\psi_{h,0}\rangle\right|^2 . \tag{2.12}$$

Constant R includes all microscopic constants such as the dipole matrix element calculated between the Bloch functions of the conduction and valence bands, which do not depend on the pumping intensity or geometry of the structure. The overlap integral between the envelope wavefunctions $\psi_{e,0}$ and $\psi_{h,0}$ is the only parameter which does depend on the radii of the core-shell structure and on the number of the existing electron-hole pairs.

In the case of the ensemble of nanostructures the observable PL intensity is determined by the average over the ensemble number of the electron-hole pairs, which can be expressed in terms of distribution functions f_c and f_s of the core and shell radii [69]:

$$\overline{n}_L(t) = \int\limits_{\overline{r}_c-\Delta_c}^{\overline{r}_c+\Delta_c}\int\limits_{\overline{w}-\Delta_w}^{\overline{w}+\Delta_w} n_L(r_c, r_c+w, t) f_c(r_c) f_w(w)\, dr_c dw \tag{2.13}$$

where $w = r_s - r_c$ is the width of the shell, $\overline{r}_c$, $\overline{w}$ are average values of the respective quantities, and Δ_c and Δ_w determine their maximum and minimum values used for numerical evaluation of the respective integrals.

The normalized PL intensity, I_{PL}, at a given photon energy, is defined by the rate

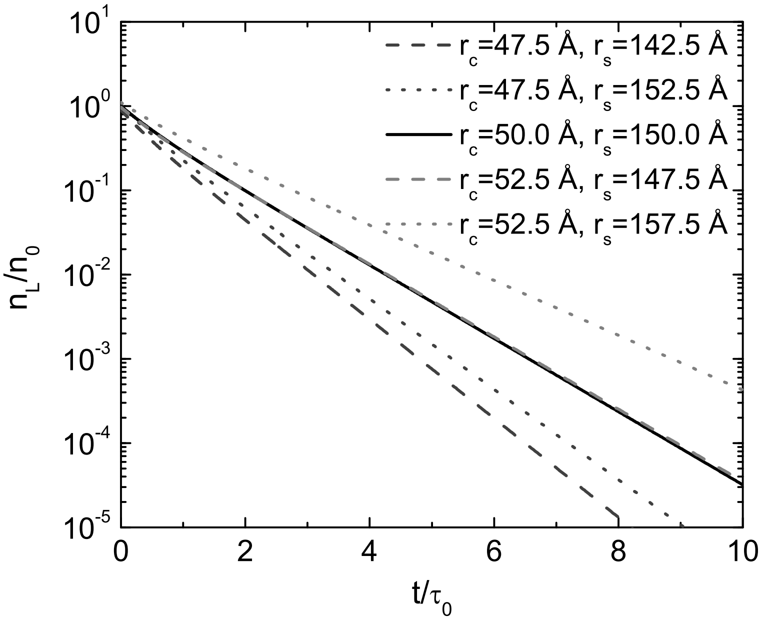

Figure 2.4: Time dependence of the normalized population of the ground sub-bands of the ZnTe/ZnSe type II core-shell quantum wires for different geometrical parameters of the structure. The solid black curve corresponds to the structure with core radius 50 Å and shell radius 150 Å. The light and dark grey dashed and dotted curves correspond to the variation of the core and shell radii. The time scale is normalized by τ_0 - calculated lifetime from the tail of the population dynamics of the structure ($r_c = 50$ Å and $r_c = 150$ Å).

of change of the average number of electron-hole pairs [69]:

$$I_{PL}(t) = -\frac{1}{\overline{n}_L(0)}\frac{d\overline{n}_L(t)}{dt}, \tag{2.14}$$

where $\overline{n}_L(0)$ is an average concentration of the carriers at initial moment of time $t = 0$. If one takes into account the dependence of the decay time τ on the concentration n_L, the solution of equation Eq. (2.11) is no longer given by an exponential function, and can only be found numerically. In order to characterize this solution it is convenient to introduce a quantity

$$\tau_0 = \lim_{n_L \to 0} \tau(n_L, \overline{r}_c, \overline{r}_s).$$

This parameter characterizes the decay rate at vanishingly small concentration of the carriers (the flat band condition) in a structure with average geometric parameters. With the use of this quantity one can introduce the dimensionless quantity, $\eta(n_L, r_s, r_c)$ defined as

$$\eta(n_L, r_c, r_s) = \frac{\tau}{\tau_0}.$$

This quantity does not depend on microscopic characteristics of the materials constituting the structure (represented by factor R in Eq. (2.12)), and only retains dependence on the excitation intensity and the radii of the core and the shell. To illustrate the effect of the difference in the core-shell radii on population dynamics we solved Eq. (2.11) for several different values of r_c and r_s. The results of the calculations are shown in Figure 2.4, where time, t, is normalized by parameter τ_0 calculated at the radii values $r_c = 50$ Å and $r_s = 150$ Å. The chosen values of the parameters correspond to typical colloidal quantum wire systems [83]. The curves shown in Figure 2.4 are characterized by different initial densities, which is due the fact that for wires with different cross-sections the linear density will differ even if the respective volume densities are the same. For all initial densities in these calculations the quasi-Fermi levels are below the first excited states for both electrons and holes. These calculations demonstrate that even small changes in the geometry of the system affect the decay rate of the population so that in realistic samples the distribution of radiative rates due to size dispersion of the structures significantly affects the PL decay.

In order to find the time dependence of PL in this case we need to evaluate the following expression

$$I_{PL}(t) = -\frac{1}{\overline{n}_L(0)\tau_0} \int\limits_{\overline{r}_c-\Delta_c}^{\overline{r}_c+\Delta_c} \int\limits_{\overline{w}-\Delta_w}^{\overline{w}+\Delta_w} \frac{n_L(t, r_c, r_c + w)}{\eta(t, r_c, r_c + w)} f_c(r_c) f_w(w) dr_c dw \tag{2.15}$$

which requires solving Eq. (2.14) for large number of different values of r_s and w randomly chosen from a specified distribution. We will assume that r_c and w are independent random Gaussian variables with variances determined by the growth technology. This description of the radii is consistent with manufacturing process of the colloidal wires [83]. Standard deviations, $\sigma_{(c,w)}$ for both distributions is defined in terms of Δ_c and Δ_w as $\Delta_{c,w} = 3\sigma_{c,w}$, while $\Delta_{c,w}$ are determined via relative maximum deviation $\Delta_r = \Delta_c/\overline{r}_c = \Delta_w/\overline{r}_w$. Results of the calculations carried out for $\Delta_r = 5\%$ and $\Delta_r = 10\%$ are presented in Figure 2.5. The grey dotted line shows the PL decay of the core-shell structure without any variations of the radii. At large time scales the tail of the decay is a single exponent as it supposed to be for almost constant lifetime. The solid black curve shows the decay of intensity at $\Delta_r = 5\%$, while the dashed curve corresponds to $\Delta_r = 10\%$. At earlier times all curves exhibit significantly fast decay, which at longer times slows down. Such a behavior is qualitatively explained by the large overlap of electron and hole wavefunctions immediately after excitation due to strong band bending caused by increased carrier density. This density decreases with time due to recombination resulting in the decrease of the electron-hole overlap and slower rate of recombination. It is interesting that in the strong band bending regime the time dependence of the luminescence appears only weakly dependent on the size disorder. At later times, however, when in the absence of disorder one would have observed a standard exponential decay, the deviations from the exponential behavior persist, but are now strongly dependent on the size dispersion. For larger disorder the time dependence of PL is much slower resulting in a longer tail of the PL. Thus our calculations reveal that the two sources of the non-exponential behavior manifest

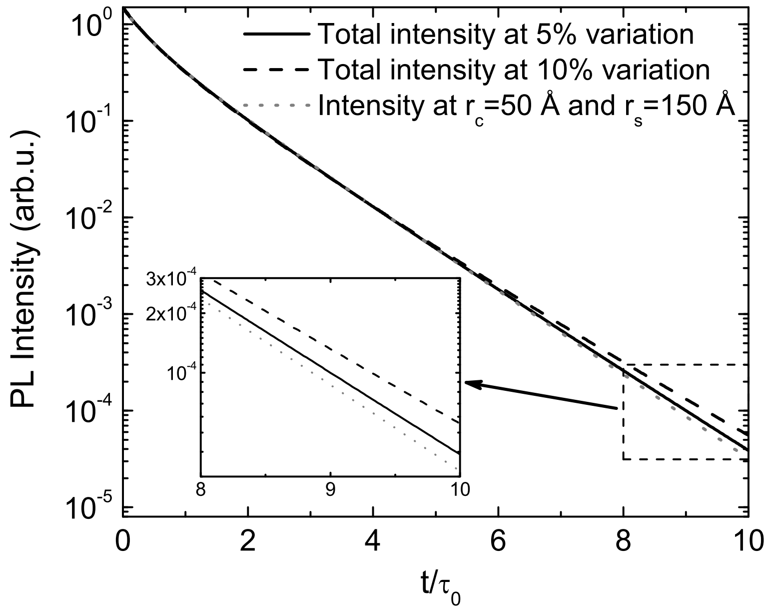

Figure 2.5: Time decay of the PL intensity of the ensemble of ZnTe/ZnSe type II core-shell quantum wires with distribution of the inner radius around core radius of 50Å and distribution of the thickness of the shell region around 100 Å. The grey dotted line shows the PL decay for the core-shell quantum wire with $r_c = 50$ Å and $r_s = 150$ Å. The solid curve shows intensity of the 5% variation of the radii. And the dashed curve represents 10% variation of the geometrical parameters.

themselves at different time scales: effects due to carrier concentration prevail at shorter times, while the disorder determines the kinetics of luminescence at longer times.

2.4 Application to vertically stacked quantum dots

Here we compare the theory presented in the previous Section with experimental results obtained for vertical stacks of quantum dots.

Applicability of this model to vertically stacked QDs, studied experimentally, requires additional justifications, which are different for electrons and holes. Electrons in this structure reside outside of the dots in the barrier material ($ZnSe$), away from the spatial regions above or below the QDs [84]. Therefore, they are virtually free to move in the vertical direction, along the whole stack, and are characterized by an effective mass typical for the bulk $ZnSe$. This behavior of electrons is confirmed by the experimental observation of the Aharonov-Bohm oscillations in magneto-optical experiments [84, 85]. The situation with holes is more complicated. First of all, in these materials the hole ground states are degenerate so that one has to distinguish between heavy holes and light holes. It is well known that in quantum wires ground state is populated mostly by light holes while in disk-like QDs the heavy hole's population is more prevalent [86, 87]. The main difference between heavy and light holes (apart of their masses) is that they obey different selection rules for interaction with light. However, this difference manifests itself mostly in polarization sensitive and magneto-optical experiments. In the phenomena discussed in this Chapter polarization effects do not play a role so that we can treat light and heavy holes in a similar way taking into account only difference in their masses and confinement potentials. Another important property of holes in stacked QDs is that, unlike electrons, they are well confined within individual QDs ($ZnTe$) with only exponential tails of their wavefunctions "leaking" outside. Using a tight-binding-like arguments one can describe holes in this situation as belonging to a narrow band of propagating states with an effective mass, which is significantly larger than the bulk effective mass, or $m^*_{z,h} \gg m^*_h$. In principle, the value of the "vertical" effective mass can be found using overlap integrals between adjacent QDs, but our calculations showed that its exact value is not important for the system considered in this work. One can think of this situation

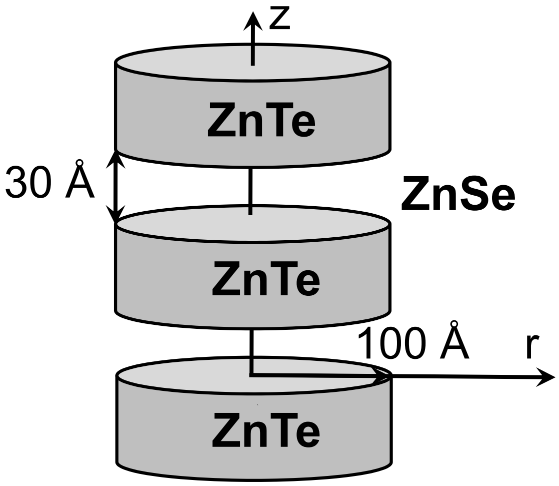

Figure 2.6: Schematic representation of the stacked quantum dots with their typical spatial parameters

as of bands of particles with infinite effective mass so that the respective densities of states become proportional to respective δ-functions with a prefactor determined by the number of QDs in the system. Since the luminescence is excited uniformly in the entire stack, we can assume that the holes are also uniformly distributed between QDs. This assumption is consistent with experimentally observed linear dependence of the PL intensity on excitation intensity [84]. In our calculations, however, we use the standard one-dimensional density of states for both holes and electrons and verify that an error due to lack of accurate knowledge of this parameter is smaller than errors caused by uncertainty of the band offsets determining confinement potentials.

The experiments were conducted with multiple stacked ZnTe/ZnSe type II QDs (Figure 2.6) grown by migration enhanced epitaxy, with growth period of 3 nm as confirmed by x-ray diffraction [88]. Details of the growth procedure can be found

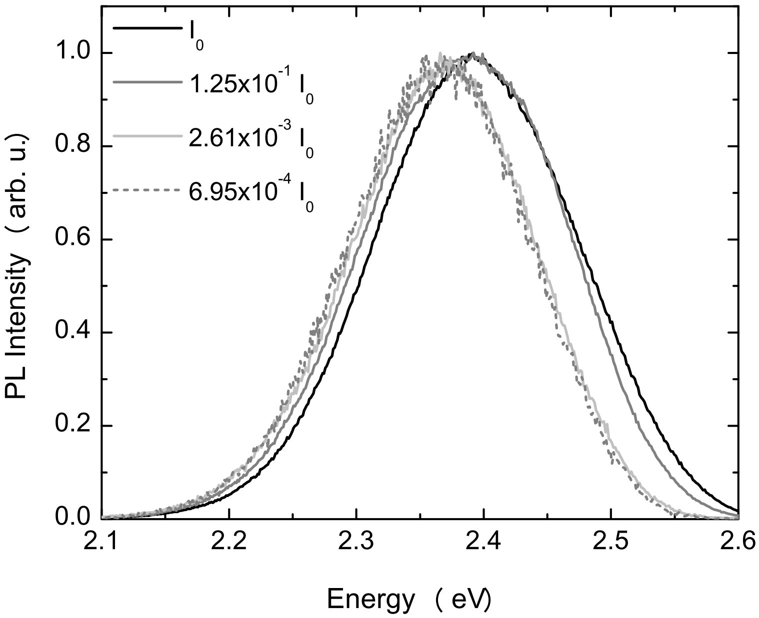

Figure 2.7: PL spectra obtained for sample with vertically stacked ZdTe/ZnSe QDs at four different intensities of excitation.

elsewhere [84, 88, 89]. The CW PL was performed in the usual configuration using the 325 nm line of a He-Cd laser, a $\frac{3}{4}$ m monochromator, and a thermoelectrically cooled GaAs photomultiplier coupled with a SR400 photon counter. The excitation intensity was varied over four orders of magnitude using neutral density filters. In the time-resolved PL measurements, a N_2 laser (4 ns pulse width) and a 500 MHz bandwidth TDS 654C oscilloscope were used for excitation and detection, respectively. All measurements were done in a closed-cycle refrigerator system at 10 K. Results of CW PL measurements are shown in Figure 2.7 for several excitation intensities.

Figure 2.8 demonstrates shift of the luminescence energy as a function of the excitation intensity. Solid squares and triangles show shift of emission frequencies corresponding to the intensity of luminescence equal to 20% of the maximum intensity on the lower and higher energy sides of the PL band, respectively. We chose to focus on these energies instead of commonly used peak energies in order to eliminate contribution to the luminescence from excitons bound to isoelectronic centers (IC) of different sizes [see Section 1.3], which are known to contribute significantly to the higher frequency side of the PL band emitted by type-II QDs [60]. Recently it has also been pointed out that this spectral region can also be affected by possible Mott's transition which might take place at high excitation intensities [90].

Focusing on frequencies from lower energy part of the PL line we are able to minimize the undesirable contribution from excitons bound to ICs or isoelectronic bound excitons. Behavior of a frequency chosen from the higher energy side of the band is shown for comparison and can be seen to be qualitatively different. This frequency shifts with increased pumping significantly faster because at higher pumping power the contribution from IBE is greater, resulting in an apparent shift toward higher frequencies. Similar effect has been also observed in magneto-PL [84], where effects associated with type II QDs were obvious only at relatively low excitation intensities.

Therefore, as a test, we compare our theoretical results obtained from Eqs. (2.8)-(2.10) with the behavior of the lower energy side of the PL. For calculations we used the same material parameters as previously (Table 2.1) with only difference that now we introduce an independent hole effective mass in the vertical direction. The value of this mass is not known, and we use it together with band offsets as a fitting parameter. Also, we take into account that in the experimental samples the radius of the core is $r_c = 100$ Å [84, 85], and the shell is virtually infinite. In order to imitate this situation theoretically we chose $r_s = 1000$ Å. Calculated results are shown by the solid line, which, as expected, reproduces proportionality of the shift to the cubic

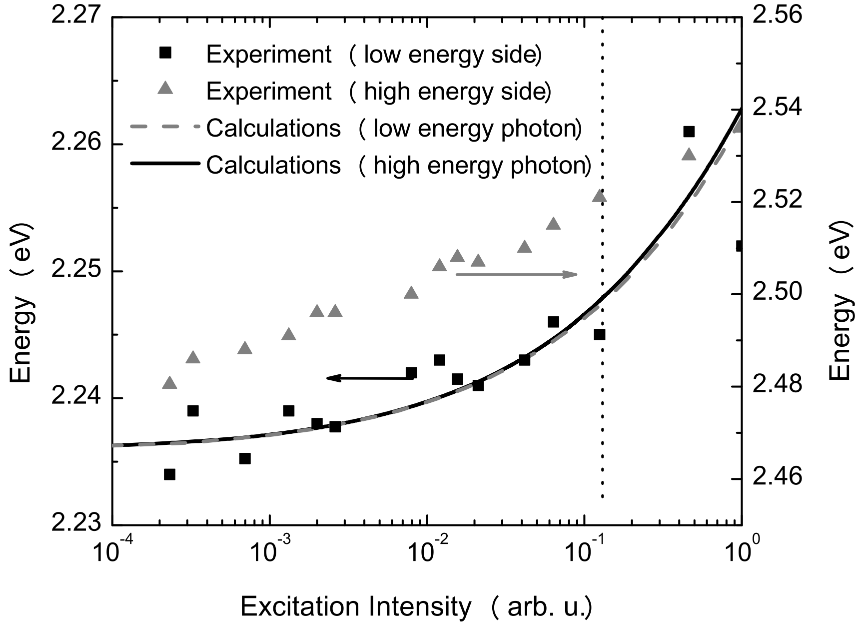

Figure 2.8: Dependence of the emission energy on the normalized excitation intensity. The solid black line represents the maximum energy (left vertical axis) of the electron-hole transition between quasi-Fermi energy levels, while the grey dashed line corresponds to the minimum energy of the band-to-band transition. The black squares correspond to the experimental emission energy (left vertical axis) taken at 20% height of the peak on the lower energy side. The grey triangles show the energy (right vertical axis) taken at the same height, but from the higher energy side of the PL spectra. The vertical dotted line shows excitation intensity ($I^{exc} \sim n_L^2$) for which electron quasi-Fermi energy level reaches the first excited state.

root of the pumping intensity and can be fitted to provide a good agreement with the experimental results.

Inset of Figure 2.9 shows normalized time-resolved PL at 2.385 eV (lower energy side of the PL) for three different excitation intensities. At the lowest excitation intensity the PL curves exhibits a decay that is close to a single exponential, but doesn't appear to be exact one. The PL decay obtained at higher excitation intensities is significantly non-exponential in agreement with previous experiments [57, 60, 61] and our theoretical results presented in Figure 2.5.

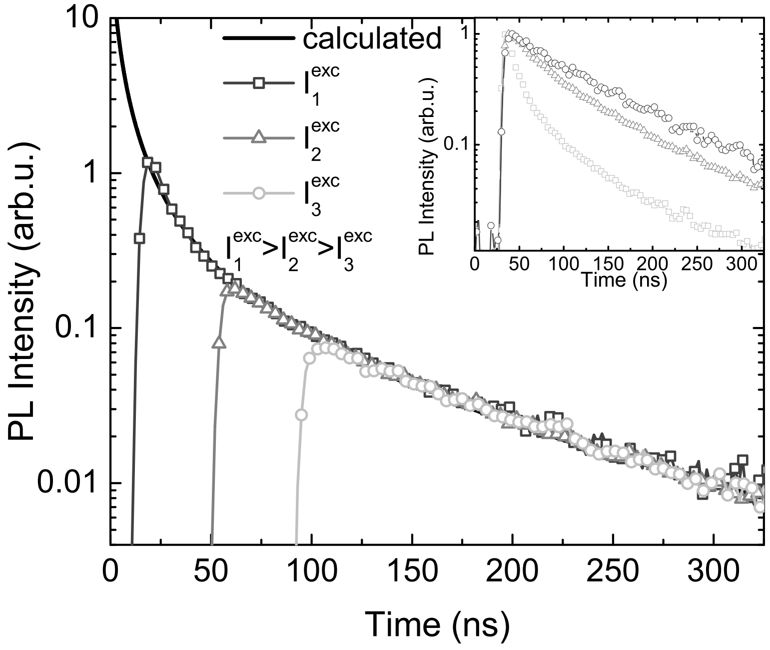

Figure 2.9: Time dependence of the PL intensity for different excitation intensities. The solid line corresponds to the intensity obtained from Eq. (2.14) with 5% variation of the core radius r_c around 100 Å. Symbols show measured time-resolved PL for three different excitation intensities. The time scale is for data obtained at the highest excitation intensity. The inset shows these decays as normalized curves (the time scale is in reference to the laser pulse for each intensity).

The three curves shown in inset of this figure can be re-scaled and plotted as a single curve. Indeed, the higher pumping power creates the larger concentration of the carriers at $t = 0$. However, at some later instant t_1 this concentration, which continuously decreases, will become equal to the initial concentration of the carriers at the lower pumping. Therefore, by simply shifting the point $t = 0$ to $t = t_1$ the respective lower pumping curve must coincide with the part of the higher pumping curve for $t > t_1$. Shifting initial times for all three curves in the inset, we obtain the master curve shown in the main Figure 2.9. One can see that points from all three different pumping intensities form a perfect single line, which shows excellent agreement with the results of the theoretical calculations depicted by a solid line. This line presents a normalized PL intensity obtained from Eq. (2.15) with $\Delta_r = 5\%$, $\overline{r}_c = 100$ Å and $\tau_0 = 140$ ns. Such a small size distribution is consistent with our main assumption that vertically stacked QDs can be treated as a one-dimensional system. Indeed, 5% size distribution is much smaller than the actual distribution of the constituent QDs, which can only be explained by averaging out of the dots diameters due to expanded nature of the wavefunctions of the carriers. A large value for τ_0 is consistent with type II band alignment in ZnTe/ZnSe heterostructures.

2.5 Discussion

It should be noted that the theoretical curve in Figure 2.9 demonstrates much faster decay of the luminescence than the curve in Figure 2.5 at earlier times, but slower decrease of intensity at the longer times. This distinction is due to difference in the shell radii used to obtain these two figures. In the case of Figure 2.5 we dealt with very wide shell layer, so that the overlap of the electron-hole wavefunctions, even though small to begin with, is much more sensitive to the changes in the band structure. It, therefore, decreases much faster with the concentration, and hence, with time, than in the case of Figure 2.5, which describes decay of PL in the sample with a much narrower shell. At the same time, the fast decrease of the overlap makes instantaneous values of the decay rate much smaller resulting in a much slower decay at longer times.

In general, the self-consistent technique employed for calculation of electronic states and dynamics of the photoluminescence in this Chapter can be adopted for the case of the QWs [57, 65] and QDs [91–93] of different types. Moreover, it allows to investigate different physical properties, such as, for example, capacitance [78, 92, 93] and conductance [92, 93].

Chapter 3

Exciton binding energy in quantum well

The ability to make heterostructures has made a tremendous impact in the area of physics of excitons. The technique of fabrication of quantum well structures, where the electrons and holes can be strongly confined in the growth direction, has allowed excitonic resonances to assume an important technological aspect due to their highly controllable nature. The main reason for the interest in excitonic resonances in quantum well structures is the enhanced binding energy of the confined electron-hole system comparable to the bulk. Simple variational calculations show that the binding energy of a 2D electron-hole system with Coulomb interaction is four times that of the 3D system. In reality, of course, a quantum well system is not a 2D system, but is a quasi-2D system. The actual binding energy is, therefore, somewhat smaller than the expected 2D value. Nevertheless, the increased binding energy allows the excitonic transitions to persist up to high temperatures.

In the present Chapter we suggest an alternative version of the variational calculations, which has a number of important advantages over the currently existing approaches. The idea of this approach is that instead of imposing a particular functional dependence on the envelope wavefunction, we present it as a combination of functions of an arbitrary form, but which depend on fewer than the total number variables. In other words, we replace an original exact wavefunction with a trial one with forced separation of variables. This idea is similar to Hartree approach to many-electron problems, where a wavefunction dependent on coordinates of all electrons is presented as a product of functions dependent on coordinates of single electrons [68]. Despite the formal analogy between the two approaches, we would like to emphasize that unlike the standard Hartree method, we do not deal with the separation of single-particle coordinates of identical particles. Instead we separate in-plane and in-growth-direction coordinates describing relative motion of an electron-hole pair. Therefore, the antisymmetrization of the wavefunction, which would result in exchange terms in regular many particle Hartree-Fock method, is not required here. Applying the variational principle to this combination of functions with separated variables we derive a system of integro-differential equations for these functions describing both the motion of electrons and holes in the direction of confinement, and the relative two-dimensional in-plane motion of the exciton. Each of these functions is determined by effective potentials that have to be determined self-consistently.

3.1 Exciton hamiltonian

We assume anisotropic parabolic dispersion law for conduction and valence bands. Throughout this Chapter we will use effective atomic units (a.u.), in which the unit of length is the three-dimensional exciton Bohr's radius $a_B = \hbar^2 \epsilon_w / (\mu_\perp^* e^2)$, the unit of energy is $E_B = \mu_\perp^* e^4 / (\hbar^2 \epsilon_w^2) \equiv 2\Re y$, and the unit of mass is a generalized reduced electron-hole mass $\mu_\perp^*$ of in-plane motion for the well material: $1/\mu_\perp^* = 1/m_e^{*w} + 1/m_{\perp h}^{*w}$. The heavy (light) hole masses for in-plane and growth direction are expressed in terms of Luttinger parameters [94] γ_1, γ_2: $m_0/m_{\perp h}^* = (\gamma_1 \pm \gamma_2)$ and $m_0/m_{\parallel h}^* = (\gamma_1 \mp 2\gamma_2)$, m_0 is the free-electron mass, top (bottom) sign corresponds to heavy (light) hole. In this notation, $m_{e,h} = m_{e,h}^* / \mu_\perp^*$. After a standard procedure of excluding the center-of-mass (COM) of the perpendicular motion in the plane of layers [3, 33], and after taking into account effective mass mismatch the excitonic Hamiltonian is given by

$$\hat{H} = E_{gap} + H_e + H_h + \frac{\mu_\perp^*}{\mu_\perp^*(z_e, z_h)} K_r + V_{reh}, \tag{3.1}$$

$$H_e = -\frac{1}{2} \frac{\partial}{\partial z_e} \frac{1}{m_e(z_e)} \frac{\partial}{\partial z_e} + V_e(z_e), \tag{3.2}$$

$$H_h = -\frac{1}{2} \frac{\partial}{\partial z_h} \frac{1}{m_{\parallel h}(z_h)} \frac{\partial}{\partial z_h} + V_h(z_h), \tag{3.3}$$

$$K_r = -\frac{1}{2} \left[\frac{\partial^2}{\partial r^2} + \frac{1}{r} \frac{\partial}{\partial r} \right], \tag{3.4}$$

where E_{gap} is gap energy, $r = \sqrt{(x_e - x_h)^2 + (y_e - y_h)^2}$ is the radius of relative motion in xy plane, $V_{e,h}$ are confining potentials on the growth direction for the electron and the hole, correspondingly, and V_{reh} is the screened Coulomb electron-hole attraction. We also assume that the ground state doesn't depend on the angle in well's plane.

Therefore, we do not include corresponding term into the Hamiltonian.

3.2 The image charges method

Quantum well and barrier materials have different band structures and, therefore, they have different static dielectric constants. This effect can be included into Eq. (3.1) by introducing image charges. The image charges method represents electric field induced by image charges placed in virtually homogenous media. Usually, for type I QW, ϵ_b is less than ϵ_w, because dielectric permeability generally behave as E_{gap}^{-1}. And, since electric field lines are more intent to penetrate through the media with lower ϵ, Coulomb attraction between electron and hole becomes less confined thus increasing exciton binding energy.

Solution of the Poisson's equation for three-layer medium gives three different forms of the potential depending on whether the carries reside inside or outside the well [95]. For the case, when both electron and hole are inside the well material, the potential is

$$V_{reh} = -\sum_{n=-\infty}^{+\infty} \frac{q^{|n|}}{\sqrt{r^2 + (nL - z_e + (-1)^n z_h)^2}} \equiv -\sum_{n=-\infty}^{+\infty} q^{|n|} W_n(r; z_e, (-1)^{1-n} z_h), \tag{3.5}$$

where

$$q^{|n|} = \left(\frac{\epsilon_w - \epsilon_b}{\epsilon_w + \epsilon_b}\right)^{|n|} \tag{3.6}$$

is the dielectric mismatch, L is the width of the well, and

$$W_n(r; z_1, z_2) = \frac{1}{\sqrt{r^2 + (z_1 + z_2 + nL)^2}}. \tag{3.7}$$

We have neglected small corrections induced by the contribution to the image charges potential coming from the electron and the hole self-energy terms. These terms depend on $z_{e,h}$ coordinates only and have Coulomb tails at large distances. They formally appear as a diagonal part of the total electrostatic energy in layered system [4, 95]. Close inspection shows that these terms exhibit unphysical singularities on the interfaces $z = \pm L/2$, which cannot be removed within given assumption about static dielectric medium without evoking to additional phenomenological parameters. The correct microscopic treatment of the problem should involve a deeper description of dynamical dispersive medium $\epsilon(\omega, k)$, which would renormalize divergencies to the well-behaved polarization-induced modifications of the confinement potential [36]. On the other hand, we mention that if we would remove the singularities by phenomenological assumptions as in Refs. [4, 95], then the induced corrections to the exciton binding energies would be order of 0.1 meV for typical III-V semiconductor materials [35]. These corrections are more than order of magnitude less than corrections due to self-consistency effects discussing in this Chapter.

3.3 The standard variational approach

For calculation of the exciton binding energy a new *self-consistent approach* was introduced. It is based on the *variational principle.* However, it is quite different from the *standard variational method* [3, 33–36]. The starting point for both methods is application of variational principle to the functional $E[\Psi]$:

$$E[\Psi] = \int \Psi^* \hat{H} \Psi dV = \min \tag{3.8}$$

with normalization condition for wavefunction

$$\int |\Psi|^2 dV = 1. \tag{3.9}$$

The next step is determined by the way of choosing of approximate wavefunction, and it is different for two approaches. The trial function $\Psi(\mathbf{r}_e, \mathbf{r}_h)$ in the standard variational method is choosing within a class of functions of predetermined analytical coordinate dependence. These functions depend on one or several variational parameters $\lambda_1, \lambda_2, ..., \lambda_n$. Then the total energy

$$E = E(\lambda_1, \lambda_2, ..., \lambda_n), \tag{3.10}$$

and numerical values of variational parameters can be found from minimization conditions

$$\frac{\partial E(\lambda_1, \lambda_2, ..., \lambda_n)}{\partial \lambda_i} = 0, \qquad i = 1, 2, ..., n. \tag{3.11}$$

The success of the method depends essentially on the choice of the trial function. It must be simple enough to lend itself easily to the calculations, but the guess about its analytical behavior must be close to the correct wavefunction in order to provide the proximity to the exact energy.

3.4 The self-consistent approach

On the other hand, the way of choosing the trial function in the *self-consistent* approach is more flexible. Instead of choosing a particular coordinate dependence of the trial function, we only assume a particular functional dependence on different coordinates for the entire wavefunction. Namely, we construct an approximate entire wavefunction $\Psi(r, z_e, z_h)$ with the help of the unknown functions $\psi_1, \psi_2, \ldots$, where each function ψ_k depends on a lesser number of variables than the entire wavefunction. Considering variations of these functions independently, from the variational principle, Eqs. (3.8) and (3.9), we obtain coupled integro-differential equations for ψ_k.

In case of a strong localization inside the quantum well (the size L of QW along z direction is smaller than three-dimensional exciton Bohr's radius) it is reasonable to use a separable form of the ground state trial function for the Hamiltonian (3.1):

$$\Psi_{exact}(r, z_e, z_h) \to \Psi_{trial}(r, z_e, z_h) = \psi(r)\chi_e(z_e)\chi_h(z_h). \tag{3.12}$$

Assuming individual normalization for every function in Eq. (3.12), we substitute Ψ_{exact} with Ψ_{trial} in Eq. (3.8). Separate variation of every function will give the system of coupled integro-differential equations

$$\begin{aligned} \left[H_e + \overline{V}_e(z_e)\right]\chi_e(z_e) &= E_e\chi_e(z_e), && (3.13)\\ \left[H_h + \overline{V}_h(z_h)\right]\chi_h(z_h) &= E_h\chi_h(z_h), && (3.14)\\ \left[\alpha K_r + \overline{V}_r(r)\right]\psi(r) &= E_X\psi(r), && (3.15) \end{aligned}$$

where $\alpha = \langle\chi_e\chi_h|\dfrac{\mu_\perp^*}{\mu_\perp(z_e, z_h)}|\chi_e\chi_h\rangle$ is a coefficient appearing as an implication of the mass mismatch effect, and the following notations are employed for the effective potentials:

$$\overline{V}_r(r) = \langle\chi_e\chi_h|V_{reh}|\chi_e\chi_h\rangle, \tag{3.16}$$

$$\overline{V}_{e,h}(z_{e,h}) = \langle\psi\chi_{h,e}|V_{reh}|\psi\chi_{h,e}\rangle. \tag{3.17}$$

The angle brackets imply that the integration is carried out over two out of three independent variables. As it can be seen, α is identically equal to unity in case of absence of mass mismatch effect and tends to this value with increasing width of the well. This happens due to the full confinement of the electron and hole wavefunctions inside the well in wide structures.

By solving system of equations (3.13), (3.14), (3.15) we obtain the best approximation for the entire wavefunction in a factorized form (3.12). The total energy of the system is given by Eq. (3.8). Averaging Eqs. (3.13)-(3.15) and adding them together gives us the following expression for the total energy:

$$E = \langle \Psi | \hat{H} | \Psi \rangle = E_e + E_h + E_X - \langle \chi_e | \overline{V}_e | \chi_e \rangle - \langle \chi_h | \overline{V}_h | \chi_h \rangle . \tag{3.18}$$

The electrostatic term describing interaction between the electron and the hole is added three times and should be subtracted twice. This substraction is leading to the renormalization of the total energy value due to the non-separability of the Hamiltonian. Thus the total energy is not just a sum of the exciton binding energy and the electron and the hole confining energies as follows from Eq. (1.3).

In order to obtain solution for Eqs. (3.13)-(3.15) we apply the method of successive approximations shown in Figure 3.1. For strong localization of exciton inside the quantum well, the corrections to the single-particle energies, as the results of interaction terms $\overline{V}_{e,h}(z_{e,h})$, are small (this is confirmed by subsequent calculations). Therefore, we neglect their contributions at zero-order approximation by setting $\overline{V}_{e,h}^{(0)} = 0$ and solving the equations

$$H_{e,h} \chi_{e,h}^{(0)}(z) = E_{e,h}^{(0)} \chi_{e,h}^{(0)} . \tag{3.19}$$

Solving this equation we are able to find a zero order approximation eigenfunctions $\psi_{e,h}^{(0)}(z_{e,h})$, which should be substituted into Eq. (3.16) in order to find $\overline{V}_r^{(0)}(r)$, a zero approximation for $\overline{V}_r(r)$:

$$\overline{V}_r^{(0)}(r) = \langle \chi_e^{(0)} \chi_h^{(0)} | V_{reh} | \chi_e^{(0)} \chi_h^{(0)} \rangle \tag{3.20}$$

The next step is to put obtained effective potential into Eq. (3.15):

$$\left[\alpha K_r + \overline{V}_r^{(0)}(r) \right] \psi^{(0)}(r) = E_X^{(0)} \psi^{(0)}(r) \tag{3.21}$$

The physical meaning of Eq. (3.21) is the formation of a two-dimensional exciton by effective electron-hole attraction. This effective interaction is a quantum-mechanical average of the Coulomb potential with confinement wavefunctions.

The calculated a zero-order wavefunction approximations $\psi_r^{(0)}(r)$, $\chi_{e,h}^{(0)}(z_{e,h})$ then placed into Eq. (3.17) in order to compute a correction to the QW electron and hole confined potentials $\overline{V}_{e,h}^{(1)}(z_{e,h})$:

$$\overline{V}_{e,h}^{(1)}(z_{e,h}) = \langle \psi^{(0)} \chi_{h,e}^{(0)} | V_{reh} | \psi^{(0)} \chi_{h,e}^{(0)} \rangle. \tag{3.22}$$

which, again, should be substituted into Eq. (3.13) and (3.14), repeating all previous steps, until the effective potentials are self-consistent to a high order of accuracy. In other words, until the following condition is satisfied:

$$\langle \psi^{(n)} | \overline{V}_r^{(n)} | \psi^{(n)} \rangle \approx \langle \chi_e^{(n)} | \overline{V}_e^{(n)} | \chi_e^{(n)} \rangle \approx \langle \chi_h^{(n)} | \overline{V}_h^{(n)} | \chi_h^{(n)} \rangle. \tag{3.23}$$

The system of equations (3.13)-(3.22), including the convergency condition (3.23), represents the complete set of equations required to find the minimum of the total

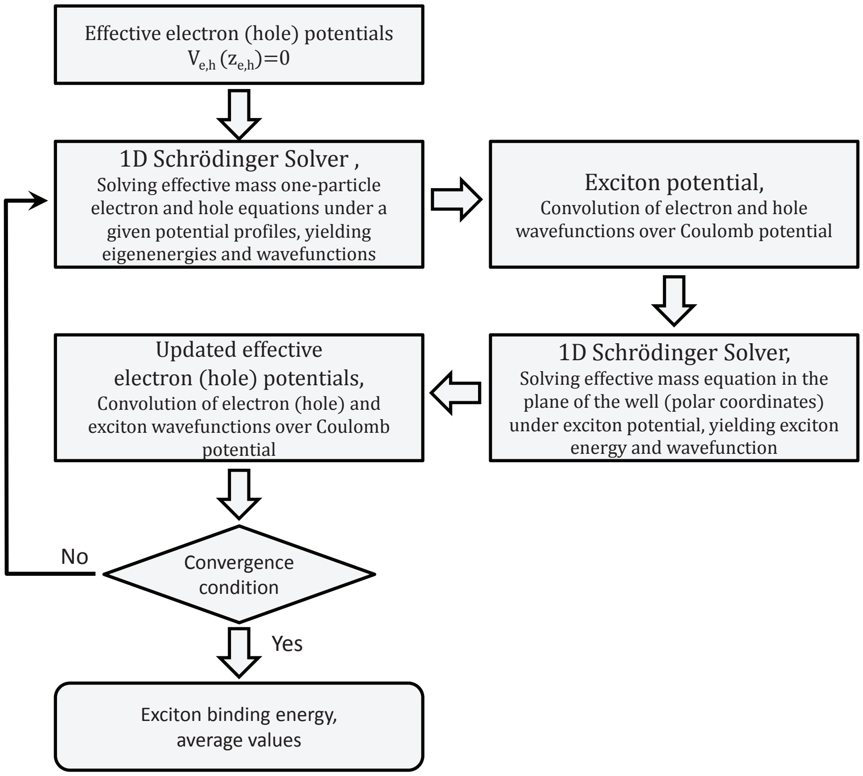

Figure 3.1: Flow chart of the method of successive approximations.

energy for the Hamiltonian (3.1) for the factorized form of the trial function Ψ (3.12). The details of calculations of the effective potentials (3.16), (3.17) are given in Appendix A.

The procedure described above is written in general form and can be applied to any configuration of well and barriers. Such important effects as valence-band mixing, non-parabolicity of the conduction band or even influence of external electric field can be also added to the model.

From computational point of view this scheme is very effective and reliable because at each step of iterations we only need to solve one-dimensional differential equations and carry out integrations. The self-consistency of our calculations presents also an additional significant benefit because from the speed of convergence of the procedure one can assess qualitatively to what degree a given functional dependence of the trial function is close to the exact solution. For instance, in the case of very broad or ultra-narrow quantum wells, where the exact wavefunction resembles a wavefunction of a three-dimensional exciton, the suggested separation of variables cannot represent this function too well, and one should expect a slow convergence of the iterations. On the other hand, for the wells of moderate thickness, where the quasi-two-dimensional nature of the excitons is manifested fully, the separation of variable should be a much better approximation for the exciton wavefunction, and our self-consistent procedure should converge much faster. Our calculations confirm this assertion.

As it was already mentioned in the Introduction, there have been previous attempts to treat the Coulomb term in Hamiltonian (3.1) in a self-consistent manner. For instance, in Ref. [72] and Refs. [43, 44] self-consistent treatment was used to compute the single-particle wavefunctions. However, for calculation of the radial, “excitonic”, part of the wavefunction the “traditional” non-self-consistent variational method was employed. Unlike those earlier works, in current calculations we extend self-consistent treatment to all three factors of the trial function, thus carrying out fully self-consistent calculations.

Finally we would like to refer to another work where the same equations as Eqs. (3.13)-(3.15) were derived independently based on a slightly different considerations and without taking into account the effect of dielectric and mass mismatches [5]. We will compare our calculations with the results of this work later in Section 3.6.3.

3.5 Exciton in δ-functional shallow well

In order to check the consistency of our derivations we applied our method to the δ-functional shallow well, which we define as a well, where exists only one bound state for both electrons and holes. We are assuming that there are no mismatches between well and barrier materials.

3.5.1 Energies and wavefunctions

In general, the energy spectrum of the quantum well with height U and finite length L is $E_{n-1} = \pi^2 x_n^2/(2mL^2)$, where x_n are the roots of the following transcendental equation:

$$\begin{aligned} x &= n - 2/\pi \arcsin\left(\frac{\pi}{Lu_0}x\right), \quad n = 1, 2, \ldots, N \\ n-1 &\leq x_n \leq n. \end{aligned} \tag{3.24}$$

Here we introduced a corresponding wave vector $u_0 = \sqrt{2mU}$ that characterizes potential height. The number of levels in the well is given by the condition

$$N = 1 + \left[\frac{u_0 L}{\pi}\right], \tag{3.25}$$

where $[\cdots]$ denotes the integer part of the number. The condition given by Eq. (3.25) can also be interpreted as a condition of a new level appearing when the potential grows in the well. For example, the second level appears when u_0 is equal to the wave vector of the ground state in the infinite well with the same length L: $u_0 = \pi/L$.

A transcendental form of Eq. (3.24) as well as a piecewise character of the eigenfunctions present additional obstacles for further calculations of the exciton binding energies. Therefore, different approximations of the finite quantum well are often used. For a wide quantum well with several energy levels inside, the model of an infinite quantum well with a slightly larger effective length $L_{\text{eff}} = L/x_1$ is an appropriate one [3]. It gives the same ground energy and correct wavefunction behavior. However, for shallow quantum wells with one level inside, the use of this model is not justified. Indeed, for an infinite quantum well the ground state energy grows with the decrease of the well's width, while the ground state energy in the finite well has a different dependence, and tends to the finite limit U when the width tends to zero: $E_0 \longrightarrow U - U^2 L^2 m/2$.

Narrow quantum wells have a different analytical limit of the δ-functional potential [37],

$$V(z) = U - \alpha\delta(z), \tag{3.26}$$

where α is a δ-potential strength. If we define this parameter as

$$\alpha = UL_{\text{eff}} = \sqrt{\frac{2U}{m} - \frac{\pi^2 x_1^2}{m^2 L^2}} \tag{3.27}$$

where L_{eff} is chosen to match the ground state energy of the finite well problem, then the well-width range of applicability of this approximation is extended up to the moment of the appearance of the second level in the finite quantum well. For typical parameters in GaAs/AlGaAs structures it corresponds to a well size $L \approx$ 40 Å. Obviously, $L_{\text{eff}} \rightarrow L$ when L tends to zero. Figure 3.2 shows typical energy dependence on well's width for the electron in the GaAs/AlGaAs quantum well for the finite quantum well and its approximations. Comparing the behavior of curves for the ground state of the finite width well and its δ-functional approximation with strength $\alpha = UL$, one can see that δ-functional curve stays always on the left. It means that the effective length parameter, determined by Eq. (3.27) should be smaller than the actual well width, which is opposite to the case of effective infinite quantum well width. In some sense, the model of δ-functional QW is complimentary to the model of effective infinite quantum well [3] (EIQW), which is used to approximate finite QW with large widths (and/or barrier heights), when the number of levels in a well is large. Indeed, the more discrete levels exist in the QW the better the EIQW model works, but it fails, giving a wrong eigenstate dependence on L, when the well has only one level. On the other hand the δ-functional QW is not applicable for quantum wells with more than one level. The delta-functional approximation is applicable both to very narrow QW and to wells with a small band-gap offset [37], i.e. when the well width and/or the band offsets are very small so that the carrier wavefunctions are mostly in the barrier region.

For the δ-functional potential it is more convenient to count energies from the barrier band edge rather than from the bottom of the well. In terms of the total Hamiltonian (3.1) it means that the energy band gap constant is the barrier's energy band gap: $E_{gap}^{\mathrm{bar}} = E_{gap}^{\mathrm{well}} + \Delta V_e + \Delta V_h$. The energy and wavefunction of a single localized state are well-known:

$$E_{e,h} = -\frac{\kappa_{e,h}^2}{2m_{e,h}}, \qquad \chi_{e,h}(z) = \sqrt{\kappa_{e,h}}\exp(-\kappa_{e,h}|z|). \tag{3.28}$$

Parameters $\kappa_{e,h} = \alpha_{e,h} m_{e,h}$ determine the localization of wavefunctions of an electron and a hole, respectively. It is worth noting that even for a very shallow quantum well, the localization length ($\sim 1/\kappa$) might be much less than the effective Bohr radius. In

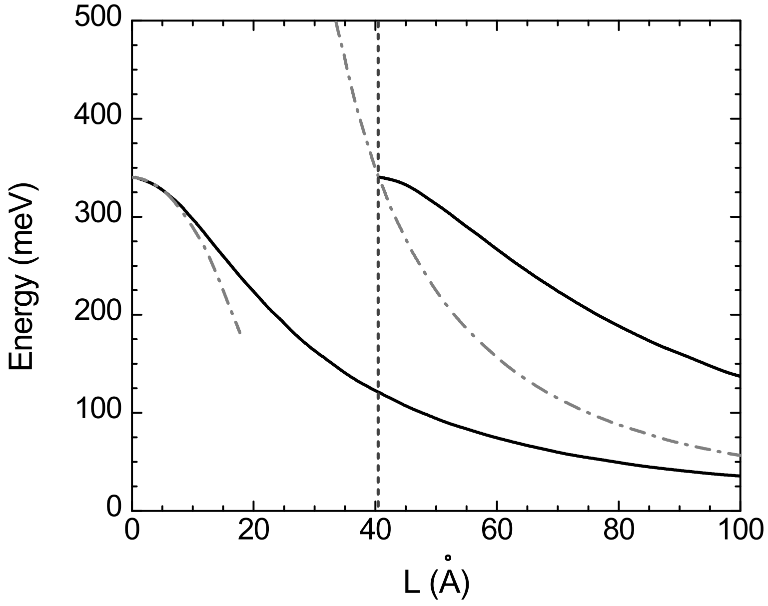

Figure 3.2: The energy levels dependence on the well's width. The ground and the first excited levels (solid lines) are shown for the finite quantum well. Dot-dashed lines show the ground state level for the infinite well of the same width and δ-functional potential (Eq. (3.26)) with $\alpha = UL$. A vertical dashed line is the well's width at which the second level in the finite quantum well appears. It shows the range of applicability of the δ-functional potential with the effective strength $\alpha = UL_{\rm eff}$. Parameters are taken for a conduction band electron in an GaAs/Al$_{0.3}$Ga$_{0.7}$As quantum well (see below in a text).

this case, we can expect a quasi-two dimensional behavior for the exciton, justifying the approximation for the mean field function in form (3.12). In the case of the GaAs/AlGaAs quantum wells, the electron (hole) localization length is smaller than Bohr's radius up to $L \approx 5$ Å.

3.5.2 Analytical expression for the exciton binding energy at first iteration

With the help of the wavefunctions (3.28), it is possible to obtain the analytical expression for the effective exciton potential $\overline{V}_r^{(0)}(r)$, which corresponds to the first

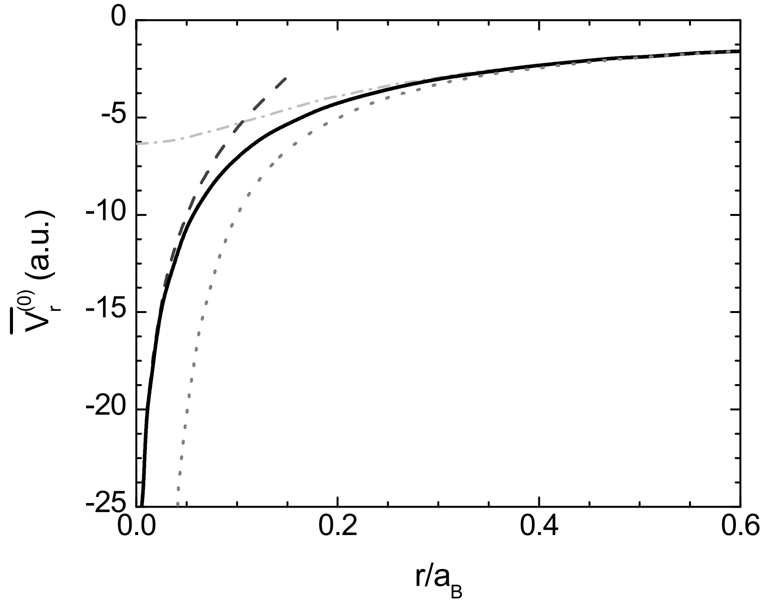

Figure 3.3: An effective self-consistent potential $\overline{V}_r^{(0)}$ profile for a two-dimensional exciton. The solid thick line represents Eq. (3.29). The dashed-dotted line is the approximation $(r^2 + d^2)^{-1/2}$, the dashed line is the logarithmic regime Eq. (3.33) for small r, the dotted line represents $1/r$ behavior. All data are for $d/a_B = 0.16$ corresponding to $L = 20$ Å finite quantum well in GaAs/AlGaAs materials.

iteration of the self-consistent procedure. The details of these calculations are given in Appendix B. The result is

$$\overline{V}_r^{(0)}(r;\kappa_e,\kappa_h) = -\frac{2\kappa_e\kappa_h}{\kappa_h^2-\kappa_e^2}\left[\kappa_h T(\kappa_e r) - \kappa_e T(\kappa_h r)\right], \tag{3.29}$$

where the function $T(\kappa r)$ is a combination of zeroth-order Struve and Neuman functions [96]:

$$T(\kappa r) = \frac{\pi}{2}\left[\mathbf{H}_0(2\kappa r) - \mathrm{Y}_0(2\kappa r)\right]. \tag{3.30}$$

The behavior of the potential (3.29) is shown in Figure 3.3 and has two regimes that are determined by the parameter

$$d = \sqrt{\frac{1}{2}\left(\frac{1}{\kappa_e^2}+\frac{1}{\kappa_h^2}\right)}. \tag{3.31}$$

This parameter has the meaning of an average electron-hole separation in the z direction. For large distances, potential (3.29) has asymptotic behavior

$$V_{\mathrm{asym}}(r) \approx -\frac{1}{\sqrt{r^2+d^2}}, \qquad r \gtrsim d. \tag{3.32}$$

At small distances, the attraction becomes stronger. It has logarithmic behavior[1]:

$$V_{\mathrm{sm}}(r) \approx \frac{1}{d}\left[\ln(r/d) - 1 + \gamma\right], \qquad r \lesssim d, \tag{3.33}$$

where $\gamma = 0.5772$.

Thus, the effective electron-hole interaction for the exciton in the quantum well starts from the true logarithmic Coulomb potential of a point charge in two dimensions that smoothly transforms at distances $r \sim d$ to the screening potential (3.32) with three-dimensional Coulomb tails. For the strong confinement $d \ll 1$ we can approximate $V_{\mathrm{eff}}(r)$ by Eq. (3.32) for all distances and take into account the logarithmic part on the next step as a perturbation.

It is interesting to note that potential (3.32) can be obtained without the self-consistent procedure from the following simple intuitive consideration. At the first step, lets us neglect the electron-hole interaction in Hamiltonian (3.1). Then, we can solve the one-dimensional one-particle Schrödinger equations in the quantum well, and find the average square of the distance between the electron and the hole as

$$d^2 = \langle \chi_e(z_e)\chi_h(z_h)|(z_e - z_h)^2|\chi_e(z_e)\chi_h(z_h)\rangle. \tag{3.34}$$

This yields the same result as Eq. (3.31). The next step in the approximation of

---

[1] For $\kappa_e \neq \kappa_h$ the series expansion of Eq. (3.33) gives $d = (\kappa_e^{-1} + \kappa_h^{-1})/2$, which is different from the definition (3.31). However, the discrepancy between these two definitions is negligible for the whole range of $\kappa_{e,h}$ under the interest.

the Hamiltonian (3.1) is to include the Coulomb attraction term, where $(z_e - z_h)^2$ is substituted by its average value $\langle\ (z_e - z_h)^2\ \rangle$.

The Schrödinger equation for a radial wavefunction in the central field (3.29) does not have an analytical solution. However, the understanding of the role played by the parameter d helps to substantially simplify calculations of the ground state energy. To obtain an approximate analytical expression for the exciton binding energy we will use the following procedure.

First of all, let us stress again that despite the fact that we consider a shallow quantum well with single particle eigenvalue inside, the strong confinement persists up to very small widths. The parameter d is a good indicator of such confinement. For example, in Table 3.1 of the next Section the data is presented for $\mathrm{Al}_{0.3}\mathrm{Ga}_{0.7}\mathrm{As}/\mathrm{GaAs}$ materials. We can see that for the well's width of 10 Å this parameter is about one quarter of the three-dimensional Bohr radius and even smaller for larger quantum wells. For the case of strong confinement, $d \ll 1$, the effective potential (3.29) can be represented by Eq. (3.32) almost everywhere. Therefore, at the first step, it is reasonable to substitute the potential (3.29) by its asymptotic form (3.32) for all distances.

Although the Schrödinger equation with the potential (3.32) also does not have an analytical solution, it was discovered that the ground state energy, obtained by the variational method for the single parameter trial function

$$\varphi_{trial} = \frac{2\exp(d/\lambda)}{\sqrt{\lambda(\lambda + 2d)}} \exp(-\sqrt{r^2 + d^2}/\lambda), \tag{3.35}$$

coincides with the exact one with excellent accuracy. To check this, a precise numerical integration of the Schrödinger equation based on Pruefer transformation and a shooting method [97] was performed. The difference in the ground state energies for the whole range of the parameter d was less than 0.01%, or $\sim 10^{-3}$ meV! Such an agreement can be explained by the fact that trial function (3.35) has a correct analytical behavior for both small and large distances r.

The expression for the ground state energy obtained for the trial function (3.35) is given by

$$E_X^{(0)}(\lambda) = -\frac{2}{\lambda}\frac{1}{1+2d/\lambda} + \frac{1}{\lambda^2}\left[1 - \frac{(2d/\lambda)^2 E_1(2d/\lambda)\exp(2d/\lambda)}{1+2d/\lambda}\right], \tag{3.36}$$

where $\mathrm{E}_1(x)$ is the exponential integral [96]. The variational parameter λ changes from 1.1 to 0.74 when the average electron-hole distance d varies from 0.11 to 0.48. The latter corresponds to the quantum well widths range from 40 Å to 5 Å for the GaAs/AlGaAs structures. The behavior of the parameter λ as a function of d is shown in the insert of Figure 3.4. At small d it has the following form:

$$\lambda \approx \frac{1}{2} + 4d + \frac{d^2}{\lambda^2}\left[4\ln\left(\frac{2d}{\lambda}\right) - 12\lambda + 4\gamma + 1\right]. \tag{3.37}$$

At small distances the effective potential (3.29) differs from Eq. (3.32). The correction to the energy due to this difference can be taken into account with the help of perturbation theory:

$$E_X^{(1)} = \langle\varphi_{trial}|\Delta V|\varphi_{trial}\rangle \approx \int_0^d \varphi_{trial}^2(r)\left[\frac{1}{d}\ln(r/d)\right] r\,dr \tag{3.38}$$

$$= -\frac{2d}{\lambda^2}\left[\frac{1}{2} - 0.557\frac{2d}{\lambda} + 0.563\left(\frac{2d}{\lambda}\right)^2 + \cdots\right]. \tag{3.39}$$

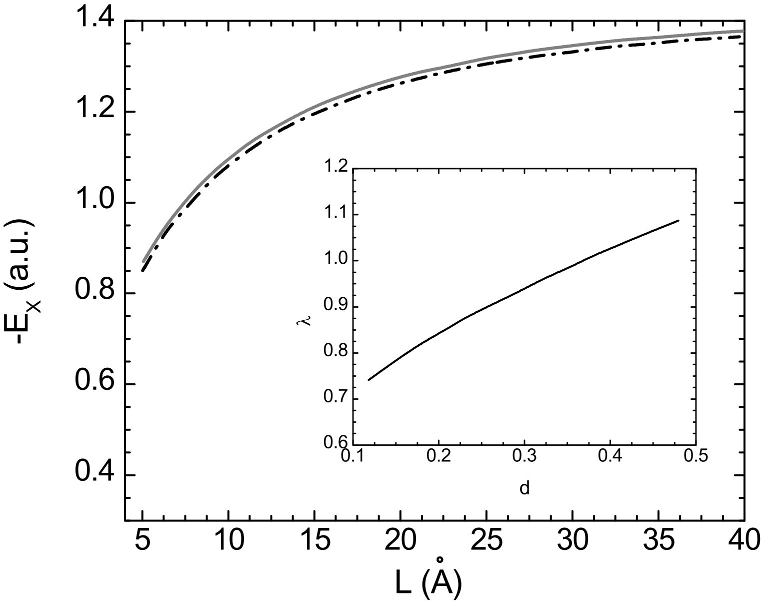

Figure 3.4: The exciton binding energies in the shallow quantum well for different well widths L. The solid line represents the two-dimensional exciton ground state, Eqs. (3.36) and (3.38) in the effective potential. The dotted-dashed line is the exciton binding energy obtained with the help of the variational method with the trial function (3.40). The insert shows the dependence of the parameter λ on the average electron-hole separation d in Eq. (3.36). Both parameters are expressed in Bohr radius units and are presented for the same range of quantum well widths.

The last but one column (E_X^{an}) of the Table 3.1 represents the final sum $E_X^{an} = E_X^{(0)} + E_X^{(1)}$ for the exciton binding energy obtained by the zero iteration of self-consistent approach.

3.5.3 Comparison with standard variational approach

We performed a numerical iteration procedure described in Section 3.4 for self-consistent coupled equations (3.13)-(3.15). The results for the exciton binding energy are presented in the last column of Table 3.1. We found a fast convergence of the iterations in the range $L = 5 \div 40$ Å of quantum well widths, where our model of shallow quantum well is applicable. Usually, it took 4-6 iterations to reach the

Table 3.1: Effective parameters of a single quantum well potentials, electron, hole and exciton binding energies (in a.u.) for different quantum well widths, L. Single particle electron and hole energies, $E^{(0)}_{e,h}$, are the initial step in the self-consistent field iterations [see Eq. (3.19)] when effective Coulomb terms $\overline{V}_{e,h}$ are omitted. These energies determine the strength parameters, $L^{e,h}_{\text{eff}}$, for corresponding δ-potentials and the average distance, d, between an electron and a hole [Eq. (3.31)]. Energies $E^{(1),(2),(3)}_X$ are the exciton binding energies obtained by variational method with the trial functions given by Eqs. (3.40), (3.41), and (3.42), respectively. The last two columns show the exciton binding energies obtained by the self-consistent approach. E^{an}_X is the analytical expression of first iteration of the self-consistent approach $E^{\text{an}}_X = E^{(0)}_X + E^{(1)}_X$ [see Eqs. (3.36), (3.38)]. E^{num}_X is the final result of the numerical iteration procedure for coupled self-consistent equations (3.13)-(3.15). The calculations are based on the following physical constants [3]: $m^*_e = 0.067m_0$, $m^*_h = 0.45m_0$, $\Delta V_e = 340$ meV, $\Delta V_h = 70$ meV, $\epsilon = 13.8$. For these parameters the effective Bohr radius is $a_B = 125$ Å and the energy atomic unit is equal to 8.33 meV.

L (Å)	L^e_{eff} (Å)	L^h_{eff} (Å)	$d(a.u.)$	$-E^{(0)}_e$	$-E^{(0)}_h$	$-E^{(1)}_X$	$-E^{(2)}_X$	$-E^{(3)}_X$	$-E^{\text{an}}_X$	$-E^{\text{num}}_X$
10	9.15	8.89	0.257	5.11	1.37	1.079	1.097	1.104	1.094	1.120
20	15.16	14.12	0.158	14.02	3.46	1.261	1.277	1.284	1.275	1.287
30	18.63	16.88	0.130	21.18	4.95	1.331	1.346	1.352	1.344	1.353
40	20.70	18.43	0.118	26.12	5.90	1.365	1.380	1.385	1.377	1.386

accuracy 0.01% for the condition of Eq. (3.23). A fast convergence confirms that a separable form of the function (3.12) is a reasonable choice for trial functions in QW with strong localization across the well.

To check the accuracy of our method we compared the results of the self-consistent approach with the results of the standard variational method for three different trial functions. These trial functions have the following forms:

$$\psi^{(1)}(z_e, z_h, r; \lambda) = \sqrt{\kappa_e \kappa_h} \exp(-\kappa_e|z_e| - \kappa_h|z_h|) \exp(-r/\lambda), \tag{3.40}$$

$$\psi^{(2)}(z_e, z_h, r; \lambda, \beta) = \sqrt{\kappa_e \kappa_h} \exp(-\kappa_e|z_e| - \kappa_h|z_h|) \exp(-\sqrt{r^2 + \beta^2}/\lambda), \tag{3.41}$$

$$\psi^{(3)}(z_e, z_h, r; \lambda, \beta) = \sqrt{\kappa_e \kappa_h} \exp(-\kappa_e|z_e| - \kappa_h|z_h|) \exp(-\sqrt{r^2 + \beta^2(z_e - z_h)^2}/\lambda), \tag{3.42}$$

The first two functions are separable, while the third one is non-separable. The first wavefunction has one variational parameter λ, and two others have two variational parameters λ and β.

The details of variational calculations are given in Appendix C. Our results and their comparison with data obtained by the standard variational procedure are presented in Table 3.1. We can see that all, even the most elaborate variational calculations, yield higher binding energies, showing that our self-consistent approach is, in fact, more accurate.

Calculations showed that already the first iteration of our approach gives lower binding energies than a variational method with separable trial functions (3.40), (3.41), while it yields energies slightly higher than the non-separable trial function. However, subsequent iterations further decrease the self-consistent ground state energy, making it the lowest one.

We would also like to mention that analytical expressions (3.36)-(3.39) for exciton binding energy give results comparable with the values obtained by variational method with separable trial functions, while avoid a numerically difficult task of finding minima of several non-polynomial functions. The additional physical information about the effective potential allows one to find one of the variational parameters of function (3.41) without minimization.

3.6 Square quantum well with mass and dielectric constant mismatches

In this Section we present the comparison of our self-consistent approach with previously published results for the square quantum well, which exhibits a mismatch of both masses and dielectric parameters.

3.6.1 Effective potentials and effect of potential renormalization

The calculations were performed for two different material systems: GaAs/$\mathrm{Al_{0.4}Ga_{0.6}As}$ and $\mathrm{In_{0.53}Ga_{0.47}As}$/InP, which have been extensively studied in the past so that our calculations can be compared with previous results. The concrete parameters of these structures used in our calculations are listed in Table 3.2.

The maximum value of the dielectric mismatch q, among a given set of the materials, corresponds to $\mathrm{In_{0.53}Ga_{0.47}As}$/InP and is equal to 0.049. Thus, we found it appropriate to truncate infinite sum by the maximum $n = 5$. All other terms will give correction to the effective potentials of the order of q^5 and this was confirmed by our calculations.

We begin discussing the results of our calculations by considering the evolution of the effective potential $\overline{V}_e(z_e)$ from one iterative step to another. This potential is a Coulomb induced modification to the rectangular shape well $V_e(z_e)$ [see Eq. (3.2)].

Table 3.2: Parameters of the materials used in the calculations: gap energy (E_{gap}), conduction band offset ($\Delta V_e/\Delta E_{gap}$), Luttinger parameters (γ_1 and γ_2), effective mass of the electron in conduction band (m_e^*), dielectric constant (ϵ), units of length (a_B) and energy (E_B). a_B and E_B are given only for the well materials. Luttinger parameters correspond to the heavy-hole effective mass. All properties of the materials are taken from the Ref. [4]

Material	E_{gap} (eV)	$\Delta V_e/\Delta E_{gap}$	γ_1	γ_2	$m_e^*(m_0)$	ϵ	q	a_B (Å)	E_B (meV)
GaAs	1.518	60%	6.85	2.10	0.0665	12.53	0.043	159	7.23
$Al_{0.4}Ga_{0.6}As$	2.163		4.67	1.17	0.0895	11.5			
$In_{0.53}Ga_{0.47}As$	0.813	40%	11.0	4.18	0.0410	13.9	0.049	291	3.56
InP	1.423		5.15	0.94	0.0803	12.6			

Initially it sets to zero, but subsequent iterations result in significant modification of its shape. Figure 3.5 shows an example of the evolution of this potential in the case of a heavy-hole exciton in a GaAs/$Al_{0.4}Ga_{0.6}As$ 120 Å wide single quantum well. One can see from the presented plots that the most changes in the shape of the effective

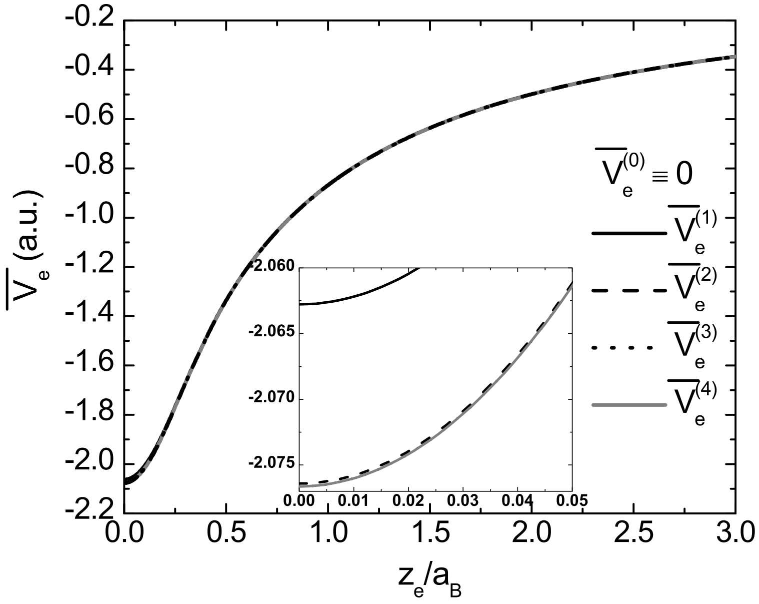

Figure 3.5: Evolution of the effective potential $\overline{V}_e(z_e)$ with every step of successive approximation for a heavy-hole exciton in GaAs/$Al_{0.4}Ga_{0.6}As$ 120Å single quantum well. Calculations are taking into account both mass and dielectric mismatches. Due to the symmetry of the potential only one half of it is shown on the graph. Solid, dashed, dotted and solid gray lines represent effective potential at the first four consecutive iterations correspondingly.

potential occur only at the first three iteration steps. Subsequent iterations result only in minor modifications of the potential and the position of the single-particle one-dimensional energy level until Eq. (3.23) is satisfied. Similar modification occurs with the hole "single-particle" potential $\overline{V}_h(z_h)$.

The main result of these modifications is down shift of the effective "single-particle" contributions to the total exciton energy. There is an additional non-trivial effect also. As a result of the self-consistent contributions, both electron and hole effective potentials acquire a long "Coulomb-like" tail at large values of z: $\overline{V}_{e,h}(z_{e,h}) \sim 1/z_{e,h}$. This renormalization significantly modifies the spectrum of "single-particle" effective energies bringing an additional number of excited discrete energy levels extending from the single-particle ground states up to the height of the barrier. An example of these modifications is shown in Figure 3.6 for the conduction band of a 45 Å wide GaAs/$\mathrm{Al_{0.4}Ga_{0.6}As}$ QW. One can see a significant lowering of the ground state energy of the electron after forth iteration of the self-consistent procedure compared to its non-self-consistent initial value. Also new energy levels arising due to the renormalization of the potential are shown (schematically).

It should be noted, however, that the conclusion about the appearance of these new excited levels has to be approached with a caution. Indeed, the variational procedure is designed for calculations of the energy of the ground state, and use of the variational procedure to study excited states in the modified potential is not fully justified. At the same time, although any new excited state needs its own self-consistent adjustment of the effective potential, it might be possible to follow the atomic-like procedure where the set of the excited orthogonal states calculated for

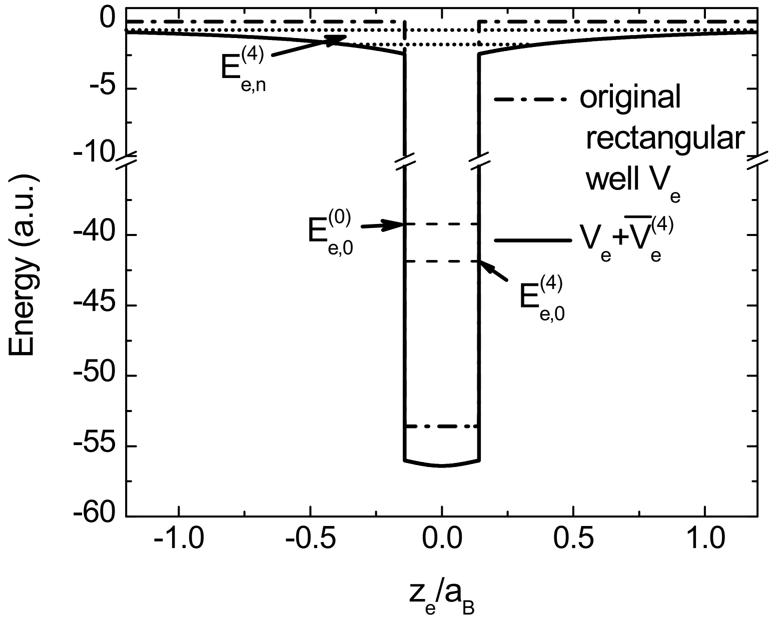

Figure 3.6: Modification of the conduction band of a heavy-hole exciton in a GaAs/Al$_{0.4}$Ga$_{0.6}$As 45 Å single quantum well due to the presence of the effective potential. Dashed dotted line presents initial profile of the conduction band and the solid line is its configuration at the fourth step. $E^{(0)}_{e,0}$ and $E^{(4)}_{e,0}$ show the position of the electron ground state energy in initial and modified potentials. $E^{(4)}_{e,n}$ are the new excited levels of the electron appearing due to the renormalization of the conduction band. These levels were not calculated and their positions are shown schematically. Valence band profile and the value of the hole's ground state energy are modifying in the same way.

the ground-state self-consistent potential. It may reduce (or may not) the number of the excited discrete levels below continuum of extended states, but this is not the main focus of the current Chapter.

The justification of this approach comes from its successes in explaining experimental results. In our case as well a justification for introducing excited states of the modified potential has to come from comparison with experiments. One of the possible experimental manifestations of these levels can be a modification of the absorption spectrum of the QW in the spectral region of the barrier absorption edge. While this question requires a separate analysis, which lies outside of the scope of

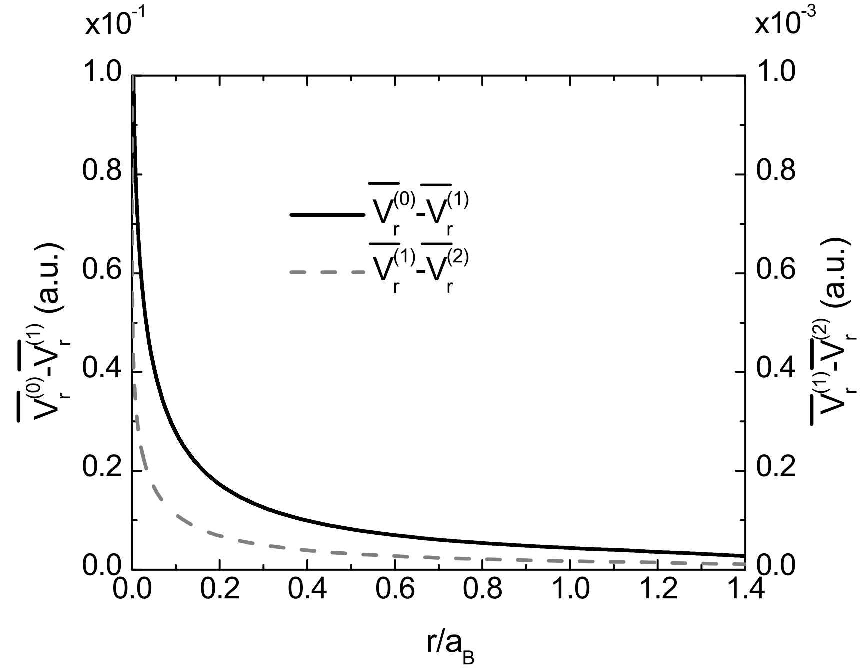

Figure 3.7: Changes in the effective potential $\overline{V}_r(r)$ with every step of successive approximation for a heavy-hole exciton in a GaAs/Al$_{0.4}$Ga$_{0.6}$As 50 Å single quantum well. Solid curve represents a difference between the value of the potential at a zero and first iterations, while the dashed line shows the difference between first and second iterations. In order to distinguish the latter curve from zero it was plotted with its own scale presented on the right-hand axes of the plot.

this Thesis, the authors of the paper [98] observed certain features in the absorption spectrum of a narrow quantum well, which could be explained by the appearance of the new excited single-particle levels in the modified potentials.

In work [5] the energies of the excitonic transitions between excited electron and hole levels were obtained from the photoluminescence spectra in a presence of the magnetic field and compared with the results of the numerical simulations for the pair of the quantum well widths.

Figure 3.7 presents the evolution of the excitonic effective potential $\overline{V}_r(r)$ with the iterations. Because of the singular behavior of the potential at $r = 0$, which results in large values of the potential at small r, the relative changes of the potential can

Table 3.3: Effective parameters describing a heavy-hole exciton in GaAs/Al$_{0.4}$Ga$_{0.6}$As 20 Å single quantum well calculated at several steps of the iteration procedure. The first column presents the number of the iteration, other columns — binding energy E_X, electron (hole) energy $E_e(E_h)$, average radius of the exciton in well's plane $\langle R\rangle$, average of z_e^2 and z_h^2, average effective potentials $\overline{V}_e, \overline{V}_h$, and $\overline{V}_r$, respectively. All energies are in terms of energy unit and all lengthes are in terms of length unit of the well material. In our case it is more convenient to count energies from the barrier band edge rather than from the bottom of the well.

n	$-E_X$	$-E_e$	$-E_h$	$\langle R\rangle$	$\langle z_e^2\rangle$	$\langle z_h^2\rangle$	$\langle\overline{V}_e\rangle$	$\langle\overline{V}_h\rangle$	$\langle\overline{V}_r\rangle$
0	1.75414	22.24994	23.87359	0.563147	0.006626	0.002002	0.00000	0.00000	3.06164
1	1.75631	25.31296	26.93540	0.562744	0.006476	0.001988	3.06436	3.06197	3.06697
2	1.75632	25.31557	26.94040	0.562748	0.006476	0.001988	3.06698	3.06697	3.06698
3	1.75632	25.31557	26.94041	0.562741	0.006476	0.001988	3.06698	3.06698	3.06698

hardly be seen directly.

Therefore, only differences between values of the potential at several consecutive iterations are presented on the Figure. One can see that the largest change occurs at the first iteration (left axis of the plot), while other consecutive iterations (right axis) result in much smaller modifications. While relative renormalization of this potential resulting from the self-consistent treatment is not very large, we will see that it results in quite significant corrections to the exciton binding energy, which justifies the necessity of complete self-consistent treatment for accurate calculations of the binding energy.

Changes of the most important effective parameters of the system with iterations for a heavy-hole exciton in a 20 Å wide GaAs/Al$_{0.4}$Ga$_{0.6}$As single quantum well structure are shown in Table 3.3. This table confirms the original conclusion based on Figure 3.5 that the main changes occur only at the first three iterations.

3.6.2 Comparison with standard variational approach

In order to compare our method with the standard variational approach we calculated the dependence of the binding energy of the heavy-hole exciton in GaAs/$Al_{0.4}Ga_{0.6}As$ and $In_{0.53}Ga_{0.47}As$/InP structures on the width of the quantum well. These calculations are compared with the results obtained by a standard variational method in Ref. [4]. The authors of that work calculated binding energy using a trial function with two variational parameters:

$$\phi(\rho, z_e, z_h) = \exp\left(-\frac{1}{a}\sqrt{\rho^2 + \lambda^2(z_e - z_h)^2}\right) u_e(z_e)u_h(z_h), \tag{3.43}$$

where $u_{e,h}(z_{e,h})$ are single-particle one-dimensional wavefunctions describing confinement of the electrons and holes in the well. The results obtained by this approach included both mass and dielectric mismatches, which were introduced almost in the same way as in current Chapter [see Section 3.2] with one exception. The authors of Ref. [4] included self-energy terms describing interaction of electrons and holes with their own images and concluded that these terms do not affect exciton energies in the materials under consideration in any significant way. Based on this conclusion we believe that it is reasonable to compare our results with those of Ref. [4] even though we have omitted the self-energy terms from our Hamiltonian.

In Figure 3.8 and Figure 3.9 we can see the dependence of the binding energy of a heavy-hole exciton in a GaAs/$Al_{0.4}Ga_{0.6}As$ and $In_{0.53}Ga_{0.47}As$/InP structures as a function of well width for several different assumptions regarding the mass and dielectric mismatches: without any mismatches, with mass or dielectric mismatch only, and with both mismatches taken into account simultaneously. This analysis

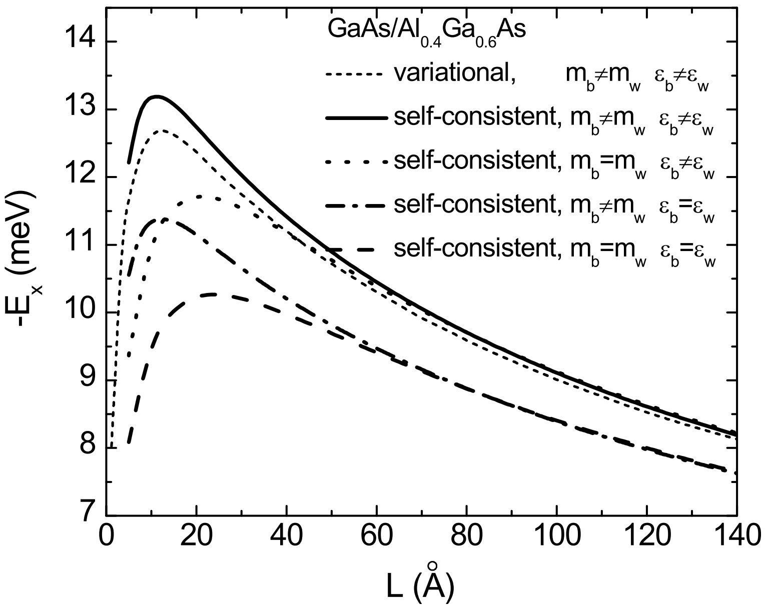

Figure 3.8: Dependence of the binding energy of a heavy-hole exciton in a GaAs/Al$_{0.4}$Ga$_{0.6}$As single quantum well on the width of the well. Curves represent different parameters of the well and barrier materials with and without mass mismatch (*mm*) and dielectric mistmatch (*dm*): *mm* and *dm* (solid line), only *dm* (dotted line), only *mm* (dashed dotted line) and dashed line doesn't have any mismatch. Comparison with the results of the standard variational approach (short dashed line) is based on data taken from Ref. [4] and includes both mismatches.

allows us not only to compare our and standard variational approaches, but also to assess effects of various discontinuities on the exciton energy. In all approximations we obtain a well known non-monotonic dependence of the binding energy on the well width with a maximum at its intermediate value. Comparing the plotted curves, however, we see that different types of discontinuities affect the energy differently. For instance, we can see that the mismatch of dielectric constants doesn't change the shape or position of the maximum of the dependence. It, however, shifts up the value of the binding energy even in for relatively wide quantum wells, where exciton should be totally confined in the well's region.

The mass mismatch across the well-barrier interface produces a qualitatively dif-

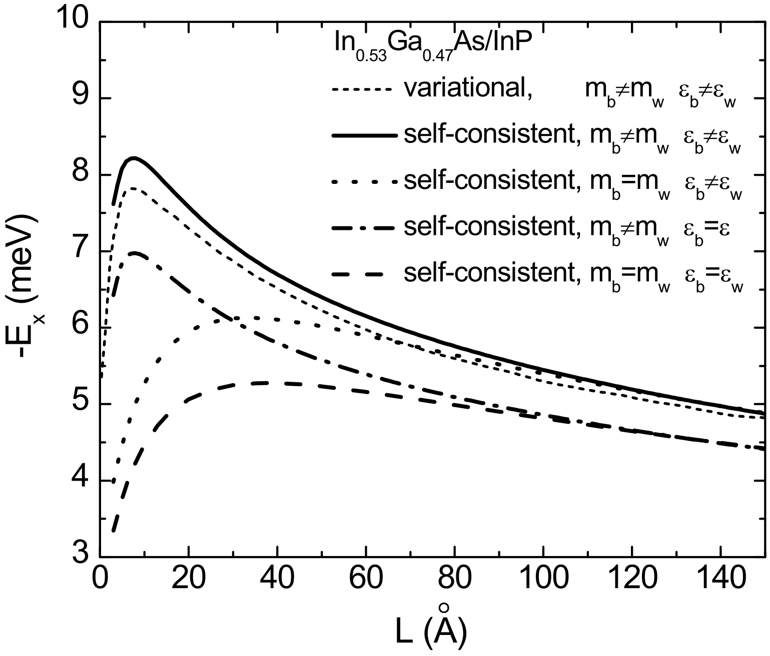

Figure 3.9: Dependence of the binding energy of a heavy-hole exciton in a $In_{0.53}Ga_{0.47}As/InP$ single quantum well on the width of the well. Curves represent different parameters of the well and barrier materials with and without mass mismatch (*mm*) and dielectric mistmatch (*dm*): *mm* and *dm* (solid line), only *dm* (dotted line), only *mm* (dashed dotted line) and dashed line doesn't have any mismatch. Comparison with the results of the standard variational approach (short dashed line) is based on data taken from Ref. [4] and includes both mismatches.

ferent effect. The form of the dependence of the binding energy on width significantly changes only at well widths comparable with the exciton Bohr radius. In this case the maximum of the curve shifts toward smaller values of the width and its shape becomes steeper close to it. Sum of these two effects results in the increase of binding energy by up to 30% at the maximum, while shifting its position to smaller widths compared to the case without any mismatch. Finally, comparing the results of our calculations with those of the standard variational approach one can see that our method gives better (meaning lower) values for the exciton energy for entire considered range of quantum well thicknesses and for both considered material systems.

3.6.3 Comparison with similar approach

Returning back to the work [5], where the same equations as ours Eqs. (3.13)-(3.15) were derived, we would like to compare the results of our calculations. The GaAs/$\mathrm{Al_{0.05}Ga_{0.95}As}$ quantum well structure was under investigation with the following properties of bulk GaAs: $m_e = 0.0665m_0$, $\gamma_1 = 6.79$, $\gamma_2 = 1.924$ and $\epsilon = 12.5$. The band offset at the heterojunction is 81.1 meV with its distribution between the conduction band and the valence band 62% and 38% respectively. The authors of that work didn't use different parameters for the $\mathrm{Al_{0.05}Ga_{0.95}As}$ barrier layer due to the low content of the Al in it.

In order to compare our calculations a linear interpolation between these parameters and parameters of the $\mathrm{Al_{0.4}Ga_{0.6}As}$ should be used and obtained values are shown in the Table 3.2. So as to find the Luttinger parameters interpolation was made for $m^*_{\perp h}$ and $m^*_{\parallel h}$ leading to the following values: $m_e = 0.06937m_0$, $\gamma_1 = 6.422$, $\gamma_2 = 1.787$ and $\epsilon = 12.4$ for the barrier layer.

Figure 3.10 shows the energy (3.10) minus the bandgap in the barrier layer. The insert represents the calculated difference in energy of excitonic transition between the system with dielectric and mass mismatches and the one without them. As one can see from this figure, our values of the energy (even without mismatch) lie lower for the wide wells than the data from Ref. [5]. This can be explained either by the replacement of the logarithmical behavior of $\overline{V}_r$ close to zero with analytical function in our case or by some assumptions made during calculations by the authors of that work. Unfortunately this is unclear from their paper. The energy is aspire to the

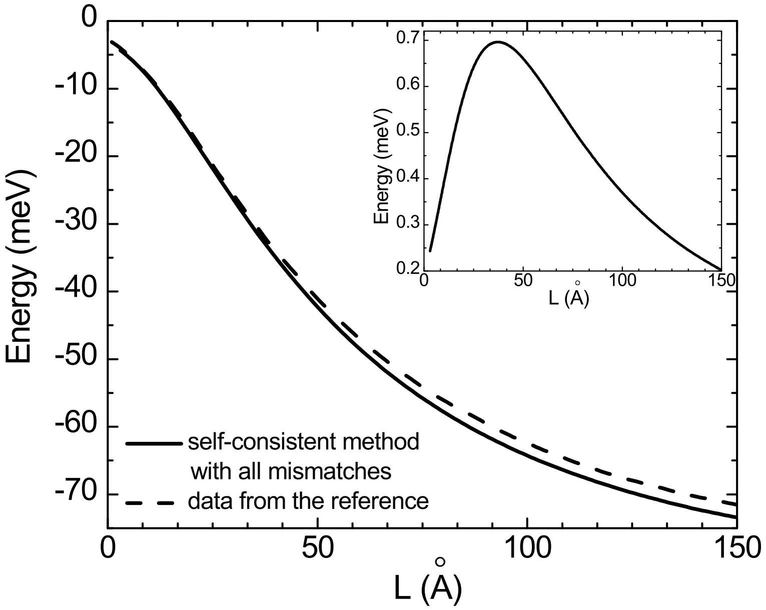

Figure 3.10: Energy of excitonic transition of a heavy-hole exciton in a GaAs/$Al_{0.05}Ga_{0.95}As$ single quantum well as a function of the quantum well width. Curves compare the results of our calculations in case of mass and dielectric mismatches (solid line) with the results from the Ref. [5] which don't have any mismatch (dashed line). The insert shows the difference of calculated energy of excitonic transition between the system with mismatches and without them.

expected value with the increasing width of the well.

Another Figure 3.11 represents the dependence of the excitonic oscillator strength, proportional to the $|\psi(0)|^2|\int_{-\infty}^{\infty}\chi_e(z)\chi_h(z)dz|^2$, as a function of the quantum well width. The solid line shows the results of our calculations including all mismatches and the dashed line is the results taken from the Ref. [5]. The graph on the insert is the calculated difference between the system with mismatches and without them. The introduced mismatches are enhancing the oscillator strength in the region of the quantum well widths up to 120 Å. This effect has place due to the strong localization of the electron and hole wavefunctions inside the well as it was described earlier in current Chapter.

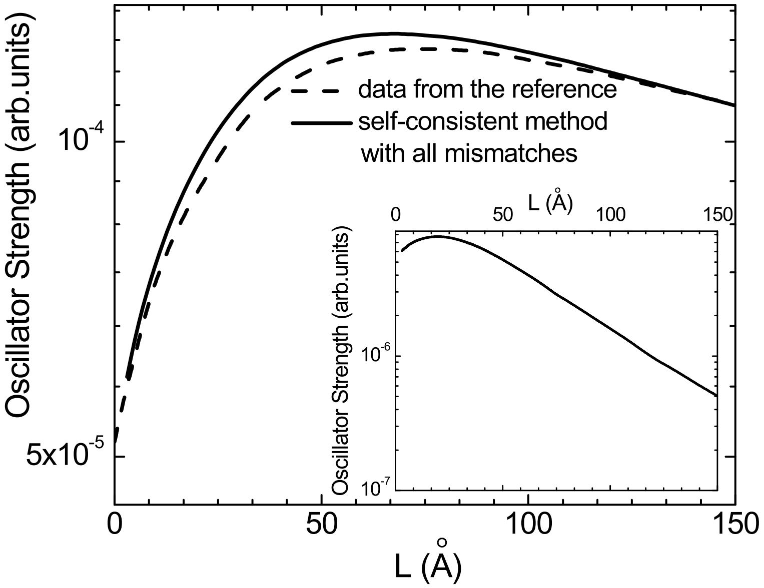

Figure 3.11: Oscillator strength of excitonic transition of a heavy-hole exciton in a GaAs/$Al_{0.05}Ga_{0.95}As$ single quantum well as a function of the quantum well width. Curves compare the results of our calculations in case of mass and dielectric mismatches (solid line) with the results from the Ref. [5] which don't have any mismatch (dashed line). The insert shows the difference of oscillator strengths between the system with mismatches and without them.

3.7 Discussion

It would be interesting to mention about some other attempts made in the past in order to treat the term responsible for Coulomb interaction in Hamiltonian (3.1) in a self-consistent manner [30, 31, 43, 44, 70, 71]. In Refs. [43, 44] was performed an incomplete self-consistent procedure for single-particle wavefunctions. Their authors choose more complicated form of the wave trial function $\Psi_{trial} = \psi(r, z_e - z_h)\chi_e(z_e)\chi_h(z_h)$ and treated its first term by the standard variational method only adjusting variational parameters. The next step was to look for self-consistent corrections to electron and hole wavefunction $\chi_{e,h}(z_{e,h})$ with the help of equations close to our Eqs. (3.13) and (3.14). In principle, it is possible to write the complete set of self-consistent integro-differential equations for this type of trial wavefunction, but the final expression for the total energy will have a more complicated form due to non-orthogonality of functions in the product for the entire trial function.

Zero approximation of another "truncated basis" approach [30, 71] is the same as our Eq. (3.21) at first step of iteration, when only the ground state confinement eigenfunctions are left. However, derivation of the Eq. (3.15) shows that it is more important than just a truncation of all but one term in the basis. One more advantage of our method is that successive iterations are taking into account the Coulomb mixing of the electron and hole subbands in a non-perturbative way providing more accurate results even in the case when this mixing is important.

The self-consistent approach described here has several advantages in comparison with the standard variational method. First of all, this method allows us to span a much larger functional space than standard variational approaches. As a result we can expect that the found energy will be lower and, hence, closer to the true value. Second, since we do not assume any particular functional form of the trial function, our method is more flexible. We can include, for instance, asymmetry, external electric or magnetic field, stress to the Hamiltonian without any need to modify the procedure. Third, the self-consistent treatment of in-plane and perpendicular motion makes this approach applicable to situations, where regular methods fail, for instance to shallow quantum wells. In addition, the renormalization of confining potentials reveals a new effect, which can not be obtained in the framework of standard variational approach. The self-consistent confinement QW potential acquires a Coulomb tail, which results in accumulation of the additional excited discrete electron and hole levels in the vicinity of barrier energies. Experimentally this should manifest itself as an additional peak in the absorption spectrum near barrier bandgap frequencies caused by Sommerfeld factor. The exchange contribution to the electron-hole potential, if needed to be taken into account, should be incorporated directly in the exciton Schrödinger equation with a help of extra spin-dependent terms [99–101].

The results discussed in this Chapter were published in the following works [102, 103].

Appendices

A Expressions for the effective potentials with dielectric constants mismatch

Placing the origin of the coordinate system into the center of the QW along z direction and using symmetry of the system we obtained the following expression for effective potential $\overline{V}_r(r)$, resulting from averaging of the screened Coulomb potential induced by image charges [95]:

$$\overline{V}_r(r) = -\left[V_1(r) + V_2(r) + V_3(r)\right], \tag{A.1}$$

where

$$
\begin{aligned}
V_1(r) &= \int\limits_0^{L/2}\int\limits_0^{L/2} dz_e\, dz_h\, F(z_e,z_h) \sum_{n=-\infty}^{\infty} q^{|n|} \left\{W_n(r;z_e,-z_h) + W_n(r;z_e,z_h)\right\}, \\
V_2(r) &= 2(1+q)\int\limits_0^{L/2}\int\limits_{L/2}^{\infty} dz_e\, dz_h\, F(z_e,z_h) \sum_{n=0}^{\infty} q^{n} \left\{W_n(r;z_e,-z_h) + W_n(r;z_e,z_h)\right\}, \\
V_3(r) &= \int\limits_{L/2}^{\infty}\int\limits_{L/2}^{\infty} dz_e\, dz_h\, F(z_e,z_h) \left\{ \frac{(1+q)}{(1-q)} \left(W_0(r;z_e,-z_h) - qW_{-1}(r;z_e,z_h)\right) \right. \\
&\qquad \left. +(1+q)^2 \sum_{n=0}^{\infty} q^n W_n(r;z_e,z_h) \right\},
\end{aligned}
\tag{A.2}
$$

and

$$
F(z_e,z_h) = \chi_e^2(z_e)\chi_h^2(z_h) + \chi_e^2(z_h)\chi_h^2(z_e), \tag{A.3}
$$

and $W_n(r;z_e,z_h)$ is defined in Eq. (3.7). The integrand in effective potential (A.1) has singularity at $r = 0, z_e = z_h$. The following coordinate transformation $\xi = z_e - z_h, \eta = z_e + z_h$ allows one to extract the divergent part. It also essentially increase the efficiency of calculations in the computational code. In new coordinates the potential has the following form:

$$
\begin{aligned}
V_1(r) = {} & \sum_{n=-\infty}^{\infty} q^{|n|} \int\limits_0^{L/2} d\eta \, \Bigg[W_{-n}(r;\eta) \int\limits_0^{\eta} d\xi \, \Phi(\xi,\eta) + W_{n-1}(r;\eta) \int\limits_0^{\eta} d\xi \, \Phi(\xi,-\eta+L) + \\
& W_n(r;\eta) \int\limits_{\eta}^{L-\eta} d\xi \, \Phi(\eta,\xi) \Bigg] , \\
V_2(r) = {} & (1+q) \sum_{n=0}^{\infty} q^n \left(V_{21n}(r) + V_{22n}(r) \right) , \\
V_{21n}(r) = {} & \int\limits_0^{L/2} d\eta \, \Bigg[W_n(r;\eta) \int\limits_0^{\eta} d\xi \, \left(\Phi(\eta,\xi+L) + \Phi(\eta,-\xi+L) \right) + \\
& W_{n+\frac{1}{2}}(r;\eta) \int\limits_0^{\eta} d\xi \, \left(\Phi\left(\xi + \frac{L}{2}, \eta + \frac{L}{2} \right) + \Phi\left(-\xi + \frac{L}{2}, \eta + \frac{L}{2} \right) \right) \Bigg] , \\
V_{22n}(r) = {} & \int\limits_{L/2}^{\infty} d\eta \, \Bigg[W_{n+\frac{1}{2}}(r;\eta) \int\limits_0^{L/2} d\xi \, \left(\Phi\left(\xi+\eta, \eta + \frac{L}{2} \right) + \Phi\left(-\xi+\eta, \eta + \frac{L}{2} \right) \right) \\
& + W_n(r;\eta) \int\limits_0^{L/2} d\xi \, \left(\Phi\left(\eta, \xi+\eta + \frac{L}{2} \right) + \Phi\left(\eta, -\xi+\eta + \frac{L}{2} \right) \right) \Bigg] , \\
V_3(r) = {} & \frac{(1+q)}{(1-q)} \int\limits_0^{\infty} d\eta \, \Bigg[W_0(r;\eta) \int\limits_{\eta}^{\infty} d\xi \, \Phi(\eta,\xi+L) + W_1(r;\eta) \int\limits_0^{\eta} d\xi \, \Phi(\xi,\eta+L) \\
& + \sum_{n=1}^{\infty} q^n \left(W_{n+1}(r;\eta) - W_{n-1}(r;\eta) \right) \int\limits_0^{\eta} d\xi \, \Phi(\xi,\eta+L) \Bigg] ,
\end{aligned}
\tag{A.4}
$$

where we put $W_n(r;\eta) \equiv W_n(r;z_e,z_h)$ and

$$
\Phi(\xi,\eta) = F\left(\frac{\xi+\eta}{2}, \frac{\eta-\xi}{2} \right) . \tag{A.5}
$$

To treat the singularity in $V_{1,2}(r)$ we split the outer integral into two parts: $\int_0^{L/2} d\eta = \int_0^{\delta} d\eta + \int_{\delta}^{L/2} d\eta$, with $\delta \ll 1$. For the first part the inner integral from $\Phi(\xi,\eta)$ can be replaced by the first several terms of its series expansion near $\eta = 0$. It results in the following approximation $\int_0^\delta d\eta\, W_n(r;\eta)(y_0 + \alpha\eta + \beta\eta^2)$. Parameters y_0, α, β are the parameters of the quadratic spline. This integral can be found explicitly and it has a logarithmic divergence at small r.

The effective potentials $\overline{V}_{e,h}(z_{e,h})$ in z-directions are free from divergencies. They can be written as follows:

$$\overline{V}_{e,h}(z_{e,h}) = \begin{cases} V^{(<)}_{e,h}(z_{e,h}), & \text{for } z_{e,h} \le \frac{L}{2}, \\ V^{(>)}_{e,h}(z_{e,h}), & \text{for } z_{e,h} \ge \frac{L}{2}, \end{cases} \tag{A.6}$$

where

$$\begin{aligned} V^{(<)}_{e,h}(z_{e,h}) = &\int\limits_0^\infty dr\, r\psi^2(r) \left(\int\limits_0^{L/2} dz_{h,e}\, \chi^2_{h,e}(z_{h,e}) \sum_{n=-\infty}^{\infty} q^{|n|} \left(W_n(r; z_{e,h}, -z_{h,e}) + W_n(r; z_{e,h}, z_{h,e})\right) \right. \\ &\left. + \int\limits_{L/2}^\infty dz_{h,e}\, \chi^2_{h,e}(z_{h,e})(1+q) \sum_{n=0}^{\infty} q^n \left(W_n(r; z_{h,e}, -z_{e,h}) + W_n(r; z_{h,e}, z_{e,h})\right) \right), \\ V^{(>)}_{e,h}(z_{e,h}) = &\int\limits_0^\infty dr\, r\psi^2(r) \left(\int\limits_0^{L/2} dz_{h,e}\, \chi^2_{h,e}(z_{h,e})(1+q) \sum_{n=0}^{\infty} q^n \left(W_n(r; z_{e,h}, -z_{h,e}) + \right. \right. \\ &W_n(r; z_{e,h}, z_{h,e})) + \int\limits_{L/2}^\infty dz_{h,e}\, \chi^2_{h,e}(z_{h,e}) \left[(1+q)^2 \sum_{n=0}^{\infty} q^n W_n(r; z_{e,h}, z_{h,e}) + \right. \\ &\left.\left. \frac{(1+q)}{(1-q)} \left(W_0(r; z_{e,h}, -z_{h,e}) - qW_{-1}(r; z_{e,h}, z_{h,e})\right) \right] \right). \end{aligned} \tag{A.7}$$

B Effective potential for 2D exciton in δ-function quantum well

The effective field for quasi 2D exciton is given by the integral

$$V_{\text{eff}}(r) = -\int\limits_{-\infty}^{\infty} dz_e \int\limits_{-\infty}^{\infty} dz_h \frac{|\chi_e(z_e)|^2 \, |\chi_h(z_h)|^2}{\sqrt{r^2 + (z_e - z_h)^2}}. \tag{B.1}$$

For a shallow quantum well approximated by the δ-function potential with eigenfunctions (3.28) it gives

$$V_{\text{eff}}(r) = -\int\limits_{0}^{\infty} dz_e \int\limits_{0}^{\infty} dz_h e^{-2\kappa_e z_e - 2\kappa_h z_h} \left[\frac{2\kappa_e\kappa_h}{\sqrt{r^2 + (z_e - z_h)^2}} + \frac{2\kappa_e\kappa_h}{\sqrt{r^2 + (z_e + z_h)^2}} \right] = V_1 + V_2. \tag{B.2}$$

After making the coordinate transformation $\xi = z_e - z_h, \ \eta = z_e + z_h$ and taking into account that

$$\int\limits_{0}^{\infty} dz_e \int\limits_{0}^{\infty} dz_h f(\xi,\eta) = \frac{1}{2}\int\limits_{0}^{\infty} d\eta \int\limits_{-\eta}^{\eta} d\xi f(\xi,\eta) = \frac{1}{2}\int\limits_{0}^{\infty} d\xi \int\limits_{\xi}^{\infty} d\eta \left[f(-\xi,\eta) + f(\xi,\eta) \right], \tag{B.3}$$

the first integration in these double integrated integrals becomes trivial and the second integration can be expressed through the function

$$T(\kappa r) = \int\limits_{0}^{\infty} \frac{\exp(-2\kappa t) dt}{\sqrt{r^2 + t^2}} = \frac{\pi}{2} \left[\mathbf{H}_0(2\kappa r) - \mathrm{Y}_0(2\kappa r) \right], \tag{B.4}$$

where $\mathbf{H}_0$ is the zeroth-order Struve function and Y_0 is the zero-order Neumann or Bessel function of the second kind [96]. Then potentials V_1 and V_2 can be expressed as

$$V_{1,2} = -\frac{\kappa_e\kappa_h}{\kappa_e \pm \kappa_h} \left[T(\kappa_h r) \pm T(\kappa_e r) \right], \tag{B.5}$$

and the final result yields Eq. (3.29):

$$V_{\text{eff}}(r; \kappa_e, \kappa_h) = -\frac{2\kappa_e\kappa_h}{\kappa_h^2 - \kappa_e^2} \left[\kappa_h T(\kappa_e r) - \kappa_e T(\kappa_h r) \right]. \tag{B.6}$$

In the case when $\kappa_e = \kappa_h \equiv \kappa$ this expression is reduced to

$$V_{\text{eff}}(r;\kappa) = -\kappa\left[T(\kappa r) - \kappa T'(\kappa r)\right], \tag{B.7}$$

where

$$T'(\kappa r) = \frac{\partial T}{\partial \kappa} = 2r\left[\frac{\pi}{2}\mathrm{Y}_1(2\kappa r) - \frac{\pi}{2}\mathbf{H}_1(2\kappa r) + 1\right]. \tag{B.8}$$

C Variational method for excitons in δ-function quantum well

Following standard procedures the envelope variational exciton wavefunction in a quantum well can be presented as a product of three terms,

$$\Psi(z_e, z_h, r; \lambda_i) = \chi_e(z_e)\chi_h(z_h)\phi(r, z_e, z_h; \lambda_i), \tag{C.1}$$

where λ_i is the set of variational parameters and ϕ is the variational wavefunction which minimizes the total energy of the Hamiltonian (3.1) without any mismatches. Two other factors $\chi_{e,h}(z_{e,h})$ are simply normalized eigenfunctions of the one-particle electron or hole Hamiltonians of the quantum well:

$$\begin{aligned}
E_{e,h}\chi_{e,h}(z_{e,h}) &= \left[-\frac{1}{2m_{e,h}}\frac{\partial^2}{\partial z_{e,h}^2} - \alpha_{e,h}\delta(z_{e,h})\right]\chi_{e,h}(z_{e,h}), \\
\chi_{e,h}(z_{e,h}) &= \sqrt{\kappa_{e,h}}\exp(-\kappa_{e,h}|z_{e,h}|), \\
\kappa_{e,h} &= m_{e,h}\alpha_{e,h}, \qquad E_{e,h} = \kappa_{e,h}^2/2m_{e,h}.
\end{aligned} \tag{C.2}$$

To obtain more confident results variational calculations were performed with the following three different trial functions ψ:

$$\begin{aligned}\psi^{(1)}(r;\lambda) &= \exp(-r/\lambda), &(C.3)\\ \psi^{(2)}(r;\lambda,\beta) &= \exp(-\sqrt{r^2+\beta^2}/\lambda), &(C.4)\\ \psi^{(3)}(r,|z_e-z_h|;\lambda,\beta) &= \exp(-\sqrt{r^2+\beta^2(z_e-z_h)^2}/\lambda), &(C.5)\end{aligned}$$

The first two functions are independent of z coordinates, while the third one is non-separable with respect to z. The first wavefunction has one variational parameter λ, and two others have two variational parameters λ and β.

The total exciton energy is the minimum of the functional

$$E = \frac{\langle\Psi|\hat{H}|\Psi\rangle}{\langle\Psi|\Psi\rangle}. \tag{C.6}$$

For the first two trial functions, which are independent of z, the functional can be further simplified. In this case, the energy can be presented as

$$E = E_e + E_h + \overline{K}/N + \overline{V}/N, \tag{C.7}$$

where

$$\begin{aligned}N &= \langle\Psi|\Psi\rangle \equiv \langle\psi(r)|\psi(r)\rangle &(C.8)\\ \overline{K} &= \langle\psi(r)|\hat{K}_r|\psi(r)\rangle \equiv \frac{1}{2}\int(\nabla\psi)^2\,dA, &(C.9)\\ \overline{V} &= -\langle\Psi|\frac{1}{\sqrt{r^2+(z_e-z_h)^2}}|\Psi\rangle \equiv \int\left(V_{\text{eff}}(r)|\psi(r)|^2\right)dA, &(C.10)\end{aligned}$$

and $dA = 2\pi r dr$. Calculations for the trial function $\psi^{(2)}$ yield

$$\begin{aligned}
N^{(2)} &= \frac{\exp(-2\beta/\lambda)\lambda(\lambda+2\beta)}{4}, \\
\overline{K}^{(2)} &= \frac{\exp(-2\beta/\lambda)}{8}\left[1+\frac{2\beta}{\lambda}-\left(\frac{2\beta}{\lambda}\right)^2 \mathrm{E}_1(2\beta/\lambda)\exp(2\beta/\lambda)\right], \\
\overline{V}^{(2)} &= -\frac{2\kappa_e\kappa_h}{\kappa_h^2-\kappa_e^2}\left[\kappa_h V(\kappa_e,\lambda,\beta)-\kappa_e V(\kappa_h,\lambda,\beta)\right], \qquad \text{(C.11)}
\end{aligned}$$

where $\mathrm{E}_1(x)$ is the exponential integral [96] and

$$V(\kappa,\lambda,\beta) = \int_0^{\pi/2}\cos(\phi)\,d\phi\int_0^{\infty}\exp(-2\kappa R\sin(\phi)-2\sqrt{R^2\cos^2(\phi)+\beta^2}/\lambda)R\,dR. \qquad \text{(C.12)}$$

For the first trial function $\psi^{(1)}(r;\lambda) \equiv \psi^{(2)}(r;\lambda,0)$ all integrals have analytical expressions:

$$\begin{aligned}
N^{(1)} &= \frac{\lambda^2}{4}, \\
\overline{K}^{(1)} &= \frac{1}{8}, \\
V(\kappa,\lambda,0) &= \frac{\lambda^2}{4}\frac{1}{1+\lambda^2\kappa^2}\left[\lambda\kappa-1+\frac{1}{\sqrt{1+\lambda^2\kappa^2}}\ln\left(\frac{1}{\lambda\kappa}\frac{\sqrt{1+\lambda^2\kappa^2}+1}{\sqrt{1+\lambda^2\kappa^2}-\lambda\kappa}\right)\right] \qquad \text{(C.13)}
\end{aligned}$$

Integrals for the non-separable trial function $\psi^{(3)}$ can be numerically estimated following the procedure described in Ref. [104].

Summary

In this work we applied self-consistent computational methods to studying optical properties of semiconductor nanostructures with one- and two-dimensional quantum confinements. In particular, we considered the problem of calculating exciton binding energies in type I quantum wells and energy levels of uncorrelated electron-hole pairs and kinetics of luminescence in type II quantum wires. The results of the latter consideration were also applied to vertical stacks of type II quantum dots with a circular cross-section and used to interpret the experimental data. The following results have been obtained:

1. In case of the cylindrical type II core-shell structures, the self-consistent technique made it possible to calculate the electron and hole states and the confining potential together with their dependencies on the carrier density. An application of this simplified model to vertically stacked ZnTe/ZnSe quantum dots allowed for comparing the experimentally measured shift of the excitation photoluminescence spectra with the theoretical prediction. The results found to be in a good agreement for the low energy part of the spectra. The discrepancy in CW photoluminescence spectra at high excitation levels is explained by

the emission of the isoelectronic bound excitons, which are always present in Zn-Se-Te systems.

2. Analysis of the photoluminescence kinetics taking into account the size dispersion of the nanostructures in a system of vertically stacked quantum dots was performed and found to be in a good agreement with the experimental observations. The observed time-resolved decay of the photoluminescence is described quantitatively, which allowed one to obtain a numerical value for a parameter characterizing overlap of the electron and hole wavefunctions in the flat band limit.

3. A model situation for the core-shell structure with finite thickness of the shell applicable to the colloidal quantum wires was discussed and investigated. It was shown that there exist two different mechanisms responsible for non-exponential behavior of time-resolved luminescence, which manifest themselves at different time scales. One of them, related to the population dependence of electron-hole energies and overlap integrals, prevails at short times, while the other one, which is due to the size dispersion of the structures, becomes more important at longer times.

4. An effective method for calculations of the characteristics of excitons in type I quantum wells is developed. The method is flexible enough to take into account such effects as dielectric constant and mass mismatches between well and barrier materials. This method is applied to two different types of quantum wells with δ and square potential profiles. Calculations showed that the suggested

method gives lower, and hence, more accurate, value of the exciton energy than traditional variational approaches for different approximations of the well and barrier parameters. Among other advantages of this approach is its versatility (the method can be immediately applied to more complex situations such asymmetrical quantum wells, wells in external fields, etc.), and computational efficiency and accuracy.

5. Besides providing more accurate values for binding energies, this approach also predicted certain modifications in the absorption spectrum of quantum wells, which can be (and may have been already) observed experimentally. This modification results from renormalization of confining electron and hole potentials due to the self-consistent treatment of the Coulomb interaction.

Bibliography

[1] O. Madelung, *Semiconductors: Data Handbook* (Springer, 2004), 3rd ed.

[2] D. Segev and S.-H. Wei, Phys. Rev. B **68**, 165336 (2003).

[3] R. Miller, A. Gossard, G. Sanders, L. Chang, and J. N. Schulman, Phys. Rev. B **32**, 8452 (1985).

[4] D. T. Thoai, R. Zimmermann, M. Grundmann, and D. Bimber, Phys. Rev. B **42**, 5906 (1990).

[5] E. A. Mulyarov, N. N. Sibel'din, M. L. Skorikov, V. A. Tsvetkov, and B. Etienne, JETP Letters **70**, 621 (1999).

[6] P. Roblin and H. Rohdin, *High Speed Heterostructure Devices* (Cambridge University Press, Cambridge, 2002).

[7] Y. Huang, X. Duan, Y. Cui, and C. M. Lieber, Nano Lett. **2**, 101 (2002).

[8] H.-J. Choi, J. C. Johnson, R. He, S.-K. Lee, F. Kim, P. Pauzauskie, J. Goldberger, R. J. Saykally, and P. Yang, J. Phys. Chem. B **107**, 8721 (2003).

[9] F. Qian, S. Gradečak, Y. Li, C.-Y. Wen, and C. M. Lieber, Nano Lett. **5**, 2287 (2005).

[10] P. S. Zory, *Quantum Well Lasers* (Academic Press, Boston, 1993).

[11] M. A. Trishenkvo, *Detection of Low-Level Optical Signals: Photodetectors, Focal Plane Arrays and Systems* (Kluwer Academic Publishers, Boston, 1997).

[12] P. Alivisatos, Nat. Biotechnol. **22**, 47 (2004).

[13] R. Dingle, W. Wiegmann, and C. Henry, Phys. Rev. Let. **33**, 827 (1974).

[14] P. M. Petroff, Appl. Phys. Lett. **41**, 635 (1982).

[15] R. Rossetti, S. Nakahara, and L. E. Brus, J. Chem. Phys. **79**, 1086 (1983).

[16] M. O. Watanabe, J. Yoshida, M. Mashita, T. Nakanisi, and A. Hojo, J. App. Phys. **57**, 5340 (1985).

[17] T. Utzmeier, G. Armelles, P. A. Postigo, and F. Briones, Phys. Rev. B **56**, 3621 (1997).

[18] G. Wannier, Phys. Rev. **52**, 191 (1937).

[19] J. Frenkel, Phys. Rev. **17**, 17 (1931).

[20] J. Frenkel, Physik Z. Sowjetunion **9**, 158 (1936).

[21] A. Mysyrowicz, D. Hulin, and A. Antonetti, Phys. Rev. Lett. **43**, 1123 (1979).

[22] M. Smith, G. D. Chen, J. Z. Li, J. Y. Lin, H. X. Jiang, A. Salvador, W. K. Kim, O. Aktas, A. Botchkarev, and H. Morkoç, Appl. Phys. Lett. **67**, 3387 (1995).

[23] A. V. Lyutetskiĭ, K. S. Borshchev, N. A. Pikhtin, S. O. Slipchenko, Z. N. Sokolova, and I. S. Tarasov, Semiconductors **42**, 104 (2008).

[24] R. Miller and D. Kleinman, J. Lumin. **30**, 520 (1985).

[25] F. Wang, Y. Wu, M. S. Hybertsen, and T. F. Heinz, Phys. Rev. B **73**, 245424 (2006).

[26] R. Cingolani, P. Prete, D. Greco, P. V. Giugno, M. Lomascolo, R. Rinaldi, L. Calcagnile, L. Vanzetti, L. Sorba, and A. Franciosi, Phys. Rev. B **51**, 5176 (1995).

[27] T. Vanhoucke, M. Hayne, M. Henini, and V. V. Moshchalkov, Phys. Rev. B **63**, 125331 (2001).

[28] R. Winkler, Phys. Rev. B **51**, 14395 (1995).

[29] A. Stahl and I. Balslev, *Electrodynamics of the Semiconductor Band Edge* (Springer, Berlin, 1987).

[30] I. Balslev, R. Zimmermann, and A. Stahl, Phys. Rev. B **40**, 4095 (1989).

[31] D. Merbach, E. Schöll, W. Ebeling, P. Mitchelm, and J. Gutowski, Phys. Rev. B **58**, 10709 (1998).

[32] R. C. Miller, D. A. Kleinman, W. T. Tsang, and A. C. Gossard, Phys. Rev. B **24**, 1134 (1981).

[33] G. Bastard, E. Mendez, L. Chang, and L. Esaki, Phys. Rev. B **26**, 1974 (1982).

[34] R. L. Greene, K. K. Bajaj, and D. E. Phelps, Phys. Rev. B **29**, 1807 (1984).

[35] L. C. Andreani and A. Pasquarello, Phys. Rev. B **42**, 8928 (1990).

[36] B. Gerlach, J. Wusthoff, M. Dzero, and M. Smondyrev, Phys. Rev. B **58**, 10568 (1998).

[37] R. C. Iotti and L. C. Andreani, Phys. Rev. B **56**, 3922 (1997).

[38] J. Kossut, J. K. Furdyna, and M. Dobrowolska, Phys. Rev. B **56**, 9775 (1997).

[39] P. Harrison, T. Piorek, W. E. Hagston, and T. Stirner, Superlatt. Microstruct. **20**, 45 (1996).

[40] S. de Leon and B. Laikhtman, Phys. Rev. B **61**, 2874 (2000).

[41] U. Ekenberg and M. Altarelli, Phys. Rev. B **35**, 7585 (1987).

[42] S. K. Chang, A. V. Nurmikko, L. A. K. J. W. Wu, and R. L. Gunshor, Phys. Rev. B **37**, 1191 (1988).

[43] J. Warnock, B. Jonker, A. Petrou, W. Chou, and X. Liu, Phys. Rev. B **48**, 17321 (1993).

[44] T. Piorek, P. Harrison, and W. Hagston, Phys. Rev. B **52**, 14111 (1995).

[45] A. Mooradian and H. Y. Fan, Phys. Rev. **148**, 873 (1966).

[46] J. Feldmann, G. Peter, E. O. Göbel, P. Dawson, K. Moore, and C. Foxon, Phys. Rev. Lett. **59**, 2337 (1987).

[47] Y. Kayanuma, Phys. Rev. B **38**, 9797 (1988).

[48] A. Mooradian and H. Y. Fan, Phys. Rev. Lett. **69**, 3393 (1992).

[49] T. Kümmell, R. Weigand, G. Bacher, A. Forchel, K. Leonardi, D. Hommel, and H. Selke, Appl. Phys. Lett. **73**, 3105 (1998).

[50] D. G. Thomas, J. J. Hopfield, and C. S. Frosch, Phys. Rev. Lett. **15**, 857 (1965).

[51] B. A. I. Monemar, CRC Crit. Rev. Solid State Mater. Sci. **15**, 111 (1988).

[52] F. Bassani, G. Iadonisi, and B. Preziosi, Rep. Prog. Phys. **37**, 1099 (1974).

[53] S. T. Pantelides, Rev. Mod. Phys. **50**, 797 (1978).

[54] V. I. Karas' and V. M. Lomako, J. Appl. Spectrosc. **34**, 680 (1981).

[55] P. L. Bradfield, T. G. Brown, and D. G. Hall, Phys. Rev. B **38**, 3533 (1988).

[56] M. Jaros, F. A. Riddoch, and L. D. Lian, J. Phys. C: Solid State Phys. **16**, L733 (1983).

[57] S. V. Zaitsev, A. A. Maksimov, I. I. Tartakovskii, D. R. Yakovlev, M. Bayer, and A. Waag, Phys. Rev. B **76**, 035312 (2007).

[58] C. Y. Jin, H. Y. Liu, S. Y. Zhang, Q. Jiang, S. L. Liew, M. Hopkinson, T. J. Badcock, E. Nabavi, and D. J. Mowbray, Appl. Phys. Lett. **91**, 021102 (2007).

[59] D. Alonso-Álvarez, B. Alén, J. M. García, and J. M. Ripalda, Appl. Phys. Lett. **91**, 263103 (2007).

[60] Y. Gu, I. L. Kuskovsky, M. van der Voort, G. F. Neumark, X. Zhou, and M. C. Tamargo, Phys. Rev. B **71**, 045340 (2005).

[61] Y. Gu, I. L. Kuskovsky, M. van der Voort, G. F. Neumark, X. Zhou, M. Muñoz, and M. C. Tamargo, Phys. Stat. Sol. (b) **241**, 515 (2004).

[62] K. Hantke, J. D. Heber, C. Schlichenmaier, A. Thränhardt, T. Meier, B. Kunert, K. Volz, W. Stolz, S. W. Koch, and W. W. Rühle, Phys. Rev. B **71**, 165320 (2005).

[63] J. Enderlein and R. Erdmann, Opt. Commun. **134**, 371 (1997).

[64] M. N. Berberan-Santos, E. N. Bodunov, and B. Valeur, Chem. Phys. **315**, 171 (2005).

[65] A. A. Maksimov, S. V. Zaitsev, I. I. Tartakovskii, V. D. Kulakovskii, N. A. Gippius, D. R. Yakovlev, W. Ossau, G. Reyscher, A. Waag, and G. Landwehr, Phys. Stat. Sol. (b) **221**, 523 (2000).

[66] R. L. Liboff, *Introductory Quantum Mechanics* (Holden-Day, San Francisco, 1980).

[67] F. Bloch, Z. Phys. **52**, 555 (1928).

[68] D. R. Hartree, Proc. Camb. Phil. Soc. **24**, 89 (1928).

[69] A. F. van Driel, I. S. Nikolaev, P. Vergeer, P. Lodahl, D. Vanmaekelbergh, and W. L. Vos, Phys. Rev. B **75**, 035329 (2007).

[70] A. L. Efros, Sov. Phys. Semicond. **20**, 808 (1986).

[71] H. Castella and J. W. Wilkins, Phys. Rev. B **58**, 16186 (1998).

[72] F. V. Kyrychenko, S. M. Ryabchenko, and Y. G. Semenov, Physica E **8**, 275 (2000).

[73] L. J. Lauhon, M. S. Gudiksen, D. Wang, and C. M. Lieber, Nature **420**, 57 (2002).

[74] Y. Wu, R. Fan, and P. Yang, Nano Lett. **2**, 83 (2002).

[75] R. G. Parr and W. Yang, *Density-Functional Theory of Atoms and Molecules* (Oxford University Press, New York, 1989).

[76] N. W. Ashcroft and N. D. Mermin, *Solid State Physics* (Saunders College, Philadelphia, 1976).

[77] J. P. Perdew and A. Zunger, Phys. Rev. B **23**, 5048 (1981).

[78] L. Wang, D. Wang, and P. M. Asbeck, Solid-State Electron. **50**, 1732 (2006).

[79] J. H. Luscombe, A. M. Bouchard, and M. Luban, Phys. Rev. B **46**, 10262 (1992).

[80] C. R. Proetto, Phys. Rev. B **45**, 11911 (1992).

[81] A. Shik, H. Ruda, and E. H. Sargent, Nanotechnology **12**, 523 (2001).

[82] N. N. Ledentsov, J. Böhrer, M. Beer, F. Heinrichsdorff, M. Grundmann, D. Bimberg, S. V. Ivanov, B. Y. Meltser, S. V. Shaposhnikov, I. N. Yassievich, et al., Phys. Rev. B **52**, 14058 (1995).

[83] A. Dong, H. Yu, F. Wang, and W. E. Buhro, J. Am. Chem. Soc. **130**, 5954 (2008).

[84] I. L. Kuskovsky, W. MacDonald, A. O. Govorov, L. Muroukh, X. Wei, M. C. Tamargo, M. Tadic, and F. M. Peeters, Phys. Rev. B **76**, 035342 (2007).

[85] I. R. Sellers, V. R. Whitesides, I. L. Kuskovsky, A. O. Govorov, and B. D. McCombe, Phys. Rev. Lett. **100**, 136405 (2008).

[86] P. C. Sercel and K. J. Vahala, Appl. Phys. Lett. **57**, 545 (1990).

[87] F. V. Kyrychenko and J. Kossut, Phys. Rev. B **67**, 4449 (2000).

[88] Y. Gong, W. MacDonald, G. F. Neumark, M. C. Tamargo, and I. L. Kuskovsky, Phys. Rev. B **77**, 155314 (2008).

[89] Y. Gu, I. L. Kuskovsky, and G. F. Neumark, *ZnSeTe rediscovered: from isoelectronic centers to quantum dots, in Wide Bandgap Light Emitting Materials and Devices* (Wiley-VCH, 2007).

[90] B. Bansal, M. Hayne, M. Geller, D. Bimberg, and V. V. Moshchalkov, Phys. Rev. B **77**, 241304 (2008).

[91] D. Jovanovic and J.-P. Leburton, Phys. Rev. B **49**, 7474 (1994).

[92] M. Stopa, Phys. Rev. B **54**, 13767 (1996).

[93] M. Macucci, K. Hess, and G. J. Iafrate, Phys. Rev. B **48**, 17354 (1993).

[94] J. C. Hensel and G. Feher, Phys. Rev. **129**, 1041 (1963).

[95] M. Kumagai and T. Takagahara, Phys. Rev. B **40**, 12359 (1989).

[96] M. Abramowitz and I. A. Stegun, *Handbook of Mathematical Functions* (Dover, New York, 1965).

[97] I. V. Ponomarev, V. V. Flambaum, and A. L. Efros, Phys. Rev. B **60**, 5485 (1999).

[98] V. Voliotis, R. Grousson, P. Lavallard, and R. Planel, Phys. Rev. B **52**, 10725 (1995).

[99] G. L. Bir and G. E. Pikus, *Symmetry and Strain-Induced Effects in Semiconductors* (Wiley, New York, 1975).

[100] Y. Chen, B. Gil, P. Lefebvre, and H. Mathieu, Phys. Rev. B **37**, 6429 (1988).

[101] L. C. Andreani and F. Bassani, Phys. Rev. B **41**, 7536 (1990).

[102] I. Ponomarev, L. I. Deych, V. Shuvayev, and A. A. Lisyansky, Physica E **25**, 539 (2005).

[103] V. A. Shuvayev, L. I. Deych, I. V. Ponomarev, and A. A. Lisyansky, Superlattice Microst. **40**, 77 (2006).

[104] P. Harrison, *Quantum wells, wires, and dots: theoretical and computational physics* (John Wiley and Sons, Chichester, 1999).